

MOLECULAR-CLOUD-SCALE CHEMICAL COMPOSITION II:  
MAPPING SPECTRAL LINE SURVEY TOWARD W3(OH) IN THE 3 MM BAND

YURI NISHIMURA<sup>1,2,3</sup>, YOSHIMASA WATANABE<sup>4,3</sup>, NANASE HARADA<sup>5</sup>, TAKASHI SHIMONISHI<sup>6,7</sup>,  
NAMI SAKAI<sup>7</sup>, YURI AIKAWA<sup>9</sup>, AKIKO KAWAMURA<sup>2</sup>, AND SATOSHI YAMAMOTO<sup>3,10</sup>

<sup>1</sup>Institute of Astronomy, The University of Tokyo, 2-21-1, Osawa, Mitaka, Tokyo 181-0015, Japan

<sup>2</sup>Chile Observatory, National Astronomical Observatory of Japan, 2-21-1, Osawa, Mitaka, Tokyo 181-8588, Japan

<sup>3</sup>Department of Physics, The University of Tokyo, 7-3-1, Hongo, Bunkyo-ku, Tokyo 113-0033, Japan

<sup>4</sup>Faculty of Pure and Applied Sciences, University of Tsukuba, 1-1-1, Tennodai, Tsukuba, Ibaraki 305-8577, Japan

<sup>5</sup>Academia Sinica Institute of Astronomy and Astrophysics, No.1, Sec. 4, Roosevelt Rd, 10617 Taipei, R.O.C., Taiwan

<sup>6</sup>Frontier Research Institute for Interdisciplinary Sciences, Tohoku University, Aramaki-zaaoba 6-3, Aoba-ku, Sendai, Miyagi 980-8578, Japan

<sup>7</sup>Astronomical Institute, Tohoku University, Aramaki-zaaoba 6-3, Aoba-ku, Sendai, Miyagi 980-8578, Japan

<sup>8</sup>RIKEN, 2-1 Hirosawa, Wako, Saitama 351-0198, Japan

<sup>9</sup>Department of Astronomy, The University of Tokyo, 7-3-1, Hongo, Bunkyo-ku, Tokyo 113-0033, Japan

<sup>10</sup>Research Center for the Early Universe, The University of Tokyo, 7-3-1, Hongo, Bunkyo-ku, Tokyo, 113-0033, Japan

ABSTRACT

In order to study a molecular-cloud-scale chemical composition, we have conducted a mapping spectral line survey toward the Galactic molecular cloud W3(OH), which is one of the most active star forming regions in the Perseus arm, with the NRO 45 m telescope. We have observed the area of  $16' \times 16'$ , which corresponds to  $9.0 \text{ pc} \times 9.0 \text{ pc}$ . The observed frequency ranges are 87–91, 96–103, and 108–112 GHz. We have prepared the spectrum averaged over the observed area, in which 8 molecular species CCH, HCN,  $\text{HCO}^+$ , HNC, CS, SO,  $\text{C}^{18}\text{O}$ , and  $^{13}\text{CO}$  are identified. On the other hand, the spectrum of the W3(OH) hot core observed at a 0.17 pc resolution shows the lines of various molecules such as OCS,  $\text{H}_2\text{CS}$ ,  $\text{CH}_3\text{CCH}$ , and  $\text{CH}_3\text{CN}$ , in addition to the above species. In the spatially averaged spectrum, emission of the species concentrated just around the star-forming core such as  $\text{CH}_3\text{OH}$  and  $\text{HC}_3\text{N}$  is fainter than in the hot core spectrum, whereas emission of the species widely extended over the cloud such as CCH is relatively brighter. We have classified the observed area into 5 subregions according to the integrated intensity of  $^{13}\text{CO}$ , and have evaluated the contribution to the averaged spectrum from each subregion. The CCH, HCN,  $\text{HCO}^+$ , and CS lines can be seen even in the spectrum of the subregion with the lowest  $^{13}\text{CO}$  integrated intensity range ( $< 10 \text{ K km s}^{-1}$ ). Thus, the contributions of the spatially extended emission is confirmed to be dominant in the spatially averaged spectrum.

*Keywords:* ISM: clouds — ISM: molecules — radio lines: ISM

1. INTRODUCTION

Recently, chemical compositions of nearby extragalactic objects have been studied by taking advantage of increased sensitivity of single-dish radio telescopes and radio interferometers. Unbiased spectral line surveys at millimeter wavelengths have been conducted toward a variety of targets; active galactic nuclei (AGNs; e.g., [Aladro et al. 2013](#)), starburst galaxies (e.g., [Martín et al. 2006](#)), and (ultra) luminous infrared galaxies ((U)LIRGs; e.g., [Martín et al. 2011](#)), as well as low-metallicity dwarf galaxies (e.g., [Nishimura et al. 2016a,b](#)). Such observations have been carried out not only for nuclear regions of nearby galaxies, but

also for positions in normal spiral arms (e.g., [Watanabe et al. 2014](#)). The chemical composition of each galaxy revealed by the spectral line survey in these studies is discussed in relation to a galaxy type, an evolutionary stage, and a physical environment. Chemical composition will be a powerful probe for star-forming activities in external galaxies, if we could link it to astrochemical concepts established in nearby star-forming regions in our Galaxy. Yet, comparison between extragalactic and galactic observations requires special attention to the large difference of the size that can be resolved in their observations. Due to the limited spatial resolution, these extragalactic studies are of a molecular-cloud scale (several ten pc), while we can readily resolve individual

dense cores ( $< 0.1$  pc) in molecular clouds for Galactic sources. Figure 1 shows the 3 mm-band spectra of the Galactic high-mass star-forming region (Orion KL) and the external galaxy (spiral arm of M51). The spectral intensity patterns are different between them. However, it is not obvious at a glance which molecular-line feature in the extragalactic spectrum reflects the internal star-forming activities. Emission from extended regions other than dense star-forming cores would contribute to the extragalactic spectrum at a molecular-cloud scale. For appropriate interpretation of extragalactic spectra in terms of star formation activities, it is very important to know the contribution of the extended component for each molecular line. Indeed, importance of such works is now being recognized (e.g., Kauffmann et al. 2017).

To fill the spatial resolution gap between galactic and extragalactic observations and understand the meaning of the molecular-cloud-scale chemical composition, the mapping spectral line survey observation toward a Galactic cloud is useful. By averaging the spectra over the large mapped area covering a whole molecular cloud, we can simulate the spectrum of Milky Way just as we observe it from the other galaxy. The mapping line survey will also provide us with a deeper insight into the origin of the molecular-cloud-scale chemical composition, because we can also study spatial distributions of molecules within a cloud. Similar mapping observations of various molecular species in the Galactic molecular clouds have recently been reported for Orion B (Pety et al. 2017) and W49A (Nagy et al. 2015), in the 84–116 GHz range and 330–373 GHz range, respectively.

This is the second paper of a series of our work on the mapping spectral line survey of molecular clouds. In the first paper (Watanabe et al. 2017), we conducted the mapping spectral line survey observation toward the active star-forming region W51. W51 is located near the tangent point of the Sagittarius arm (Sato et al. 2010). We revealed the molecular-cloud-scale chemical composition of W51, and found that it reflects a relatively diffuse part of molecular clouds rather than dense star-forming cores. In this study, we extend our work to another molecular cloud W3(OH). W3(OH) is a massive star-forming region in the Perseus arm, which is located in the outer part of our Galaxy. The Galactocentric distance is 9.95 kpc (Xu et al. 2006), and the distance from the sun is 1.95 kpc. By comparing W3(OH) with W51, we can also examine the environmental effect on the molecular-cloud-scale chemical composition.

In the W3 giant molecular cloud, the most active star-forming regions are W3 Main, W3(OH), and AFGL333 (Figure 2). These three star-forming regions are located in the eastern edge of the W3 giant molecular cloud. This structure is considered to be formed probably from materials swept up by the expansion of the W4 H II

region (Lada et al. 1978). W3(OH), the target of this mapping line survey, is an ultracompact H II region harboring many OH maser spots (Wynn-Williams et al. 1972) and the second active star-forming region after W3 Main. A size of the hot core is estimated to be  $0.02 \times 0.01$  pc (Wyrowski et al. 1999).

The W3 giant molecular cloud has been studied in various wavelengths in order to investigate its star-formation activities and evolutionary stages. Infrared maps ( $70 \mu\text{m}$ ,  $160 \mu\text{m}$ ,  $250 \mu\text{m}$ ,  $350 \mu\text{m}$ , and  $500 \mu\text{m}$ ) were obtained with *Herschel* (Rivera-Ingraham et al. 2013). The distributions of CO and atomic carbon were also reported (e.g., Sakai et al. 2006). The spectral line survey from 85 to 115 GHz was conducted toward several star-forming cores in the W3 giant molecular cloud (Kim et al. 2006). Hence, the W3 giant molecular cloud is regarded as one of the most favorable targets for molecular-cloud-scale chemical studies.

In this study, we present the result of our mapping observation toward W3(OH). Here, we focus on the molecular-cloud-scale chemical composition rather than the properties of each star-forming region. The rest of this paper is organized as follows. In Section 2, we describe the observations and data reduction. In Section 3, we show the observed spectra and line profiles, and present the distribution of key molecular species. Data analysis and discussions, including the correlation of each molecular species with  $^{13}\text{CO}$  and  $\text{HCO}^+$  and interpretations of the spatially averaged spectrum, are presented in Section 4. We also compare the spectrum of W3(OH) with those of other sources. Finally, we summarize main conclusions in Section 5.

## 2. OBSERVATIONS AND DATA REDUCTION

The observations were carried out with the 45 m radio telescope at Nobeyama Radio Observatory (NRO) in March 2015. We observed the frequency ranges of 87 – 91, 96 – 103, and 108 – 112 GHz. The half-power beam width (HPBW) of the telescope is  $20.2''$  and  $16.1''$  at 87 and 112 GHz, respectively, which correspond to 0.19 and 0.15 pc at the distance of W3 (1.95 kpc; Xu et al. 2006), respectively. We observed two orthogonal polarization signals simultaneously by using the SIS mixer receiver (TZ1), whose system temperature ranged from 130 to 180 K. The backend was the autocorrelator SAM45. The frequency resolution and bandwidth are 488.28 kHz and 1600 MHz, respectively. The line intensity was calibrated by the chopper wheel method, and a typical calibration accuracy was 20%. The antenna temperature is divided by the main beam efficiency of 0.48 and 0.41 at 87 and 112 GHz, respectively, to obtain the main beam temperature  $T_{\text{MB}}$ .

We employed the On-The-Fly (OTF) mode for the mapping observation. The center position of the

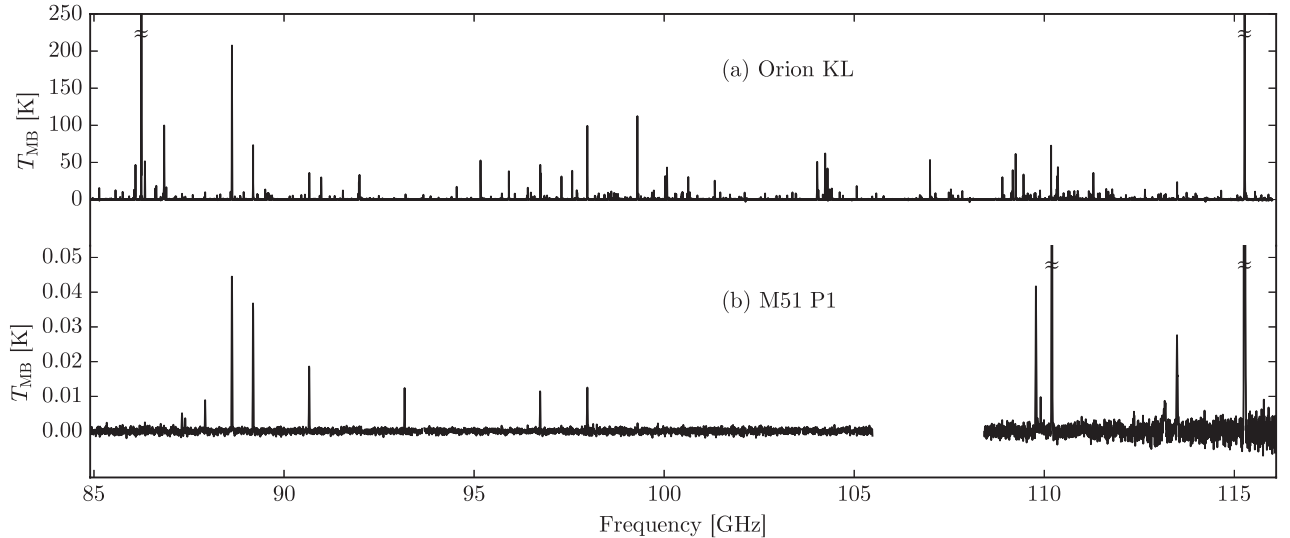


**Figure 1.** The 3 mm band spectra of (a) galactic high mass star-forming regions Orion KL (Watanabe et al. 2015, 0.04 pc resolution), and (b) external galaxies M51 P1 (Watanabe et al. 2014, 1 kpc resolution).

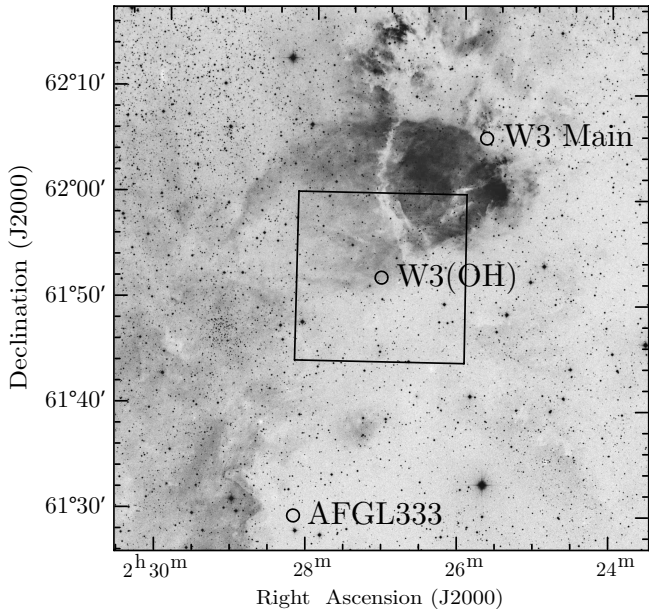


**Figure 2.** The Digitized Sky Survey image (R band; 700 nm) of the W3 region. Three star-forming clouds, W3 Main, W3(OH), and AFGL333, are indicated by circles. We observed the area enclosed by a solid black line. The Digitized Sky Survey was produced at the Space Telescope Science Institute and the images of these surveys are based on photographic data obtained using the Oschin Schmidt Telescope on Palomar Mountain and the UK Schmidt Telescope.

map is W3(OH):  $(\alpha_{J2000.0}, \delta_{J2000.0}) = (2^{\text{h}}27^{\text{m}}4.0^{\text{s}}, 61^{\circ}52'24.0'')$ . The mapping area is a square of  $16.0' \times 16.0'$  centered at W3(OH), as shown in Figure 2, which corresponds to the linear scale of  $9.0 \text{ pc} \times 9.0 \text{ pc}$ . The grid spacing for the OTF observation is  $6''$ . The total observation time was  $\sim 20$  hours. In addition to the OTF mapping, we conducted a short observation

for a few minutes toward W3(OH) (the center position of the map) with the position-switching mode. Hereafter, we refer the spectrum of this position to as a “hot core” spectrum. For both the mapping and single-point observations, the reference position was taken as:  $(\alpha_{J2000.0}, \delta_{J2000.0}) = (2^{\text{h}}29^{\text{m}}57.1^{\text{s}}, 62^{\circ}5'41.1'')$ . The telescope pointing was checked by observing the nearby SiO maser source (S Per) every hour, and the pointing accuracy was maintained to be better than  $5''$ .

The observation data were first reduced with the NRO software *NOSTAR* and *NEWSTAR*, and then detailed analyses were carried out by using our own codes. Although we scanned two orthogonal direction ( $\alpha$ - and  $\delta$ -direction) in the OTF mapping observation, we did not use the  $\delta$ -direction data for the analysis because of poor signal-to-noise ratios due to bad weather conditions. Since we convolved the image with the  $30''$  beam for analysis, the scanning effects can be negligible.

In the analysis, a baseline of the 5th-order polynomial was subtracted from each 0.2 GHz range, where the frequency resolution is 1 MHz. We identified the observed lines with the aid of the spectral line database CDMS (Müller et al. 2001; Müller et al. 2005). For the detailed analysis of each molecular line, a baseline of the 5th-order polynomial was subtracted in the velocity range from  $-150$  to  $50 \text{ km s}^{-1}$  with the velocity resolution of  $2 \text{ km s}^{-1}$ .

### 3. RESULTS

#### 3.1. Hot-core-scale and molecular-cloud-scale spectra

Figure 3 shows the “hot core” spectrum and the spectrum averaged over the full  $9.0 \text{ pc} \times 9.0 \text{ pc}$  area. The averaged spectrum is prepared by averaging the spectra of all the mapping grid points whose spacing is

much smaller than the telescope beam. The lines of CCH, HCN, HCO<sup>+</sup>, HNC, CS, SO, C<sup>18</sup>O, and <sup>13</sup>CO are strongly detected in the both spectra. In the “hot core” spectrum, the lines of C<sup>34</sup>S, CH<sub>3</sub>OH, and HC<sub>3</sub>N are also detected with relatively high intensity. Furthermore, H<sup>13</sup>CN, C<sup>33</sup>S, OCS, <sup>34</sup>SO, H<sub>2</sub>CS, CH<sub>3</sub>CCH, and CH<sub>3</sub>CN are identified in spite of the short integration time, as shown in Figure 4. On the other hand, a fewer molecular lines are detected in the averaged spectrum. Even C<sup>34</sup>S and CH<sub>3</sub>OH are marginally detected, and HC<sub>3</sub>N is absent. Individual line profiles in the spectrum averaged over the whole area are shown in Figure 5. The line parameters obtained by the Gaussian fitting

are summarized in Table 1.

Generally, brightness temperatures of the averaged spectrum are fainter than those of the “hot core” spectrum. However, intensity ratios of molecular lines between the “hot core” spectrum and the averaged spectrum are different from species to species. Using HCO<sup>+</sup> as a reference, CCH is found to be relatively strong in the averaged spectrum, while the other species such as HCN, HNC, CS, and SO are fainter. This fact may reflect the different distributions of these emissions. We will discuss this point more closely in Section 4.2. OCS, H<sub>2</sub>CS, CH<sub>3</sub>CCH, and CH<sub>3</sub>CN are detected only in the “hot core” spectrum. These species would be mainly distributed just around the star-forming region.

**Table 1.** Line parameters of the spectrum averaged over all the observed area (9.0 pc × 9.0 pc).

Molecule	Frequency (GHz)	Transition	$T_{\text{MB}}$ Peak (mK)	$v_{\text{LSR}}$ (km s <sup>-1</sup> )	$\Delta v$ (km s <sup>-1</sup> )	$\int T_{\text{MB}} dv$ (K km s <sup>-1</sup> )
CCH	87.284105	$N = 1 - 0, J = 3/2 - 1/2, F = 1 - 1$				< 0.1
CCH	87.316898	$N = 1 - 0, J = 3/2 - 1/2, F = 2 - 1$	$0.157 \pm 0.013$	$-46.6 \pm 0.2$	$5.2 \pm 0.5$	$0.95 \pm 0.03$
CCH	87.328585	$N = 1 - 0, J = 3/2 - 1/2, F = 1 - 0$	$0.072 \pm 0.018$	$-46.1 \pm 0.9$	$7 \pm 2$	$0.51 \pm 0.03$
CCH	87.401989	$N = 1 - 0, J = 1/2 - 1/2, F = 1 - 1$	$0.062 \pm 0.008$	$-47.6 \pm 0.4$	$5.9 \pm 0.9$	$0.30 \pm 0.03$
CCH	87.407165	$N = 1 - 0, J = 1/2 - 1/2, F = 0 - 1$	$0.024 \pm 0.013$	$-47.7 \pm 1.2$	$5 \pm 3$	$0.05 \pm 0.03$
CCH	87.446470	$N = 1 - 0, J = 1/2 - 1/2, F = 1 - 0$				< 0.1
HCN	88.631602	$J = 1 - 0$	$0.263 \pm 0.008$	$-46.71 \pm 0.15$	$10.6 \pm 0.4$	$3.16 \pm 0.03$
HCO <sup>+</sup>	89.188525	$J = 1 - 0$	$0.368 \pm 0.010$	$-46.85 \pm 0.08$	$5.83 \pm 0.18$	$2.37 \pm 0.02$
HNC	90.663568	$J = 1 - 0$	$0.146 \pm 0.009$	$-47.05 \pm 0.14$	$4.7 \pm 0.3$	$0.71 \pm 0.02$
C <sup>34</sup> S	96.412950	$J_F = 2_0 - 1_0$	$0.030 \pm 0.006$	$-46.6 \pm 0.6$	$5.8 \pm 1.4$	$0.148 \pm 0.019$
CH <sub>3</sub> OH	96.741375	$J_K = 2_0 - 1_0, A^+$	$0.030 \pm 0.005$	$-45.5 \pm 1.1$	$14 \pm 3$	$0.42 \pm 0.02$
CS	97.980953	$J = 2 - 1$	$0.244 \pm 0.007$	$-47.15 \pm 0.08$	$5.19 \pm 0.18$	$1.38 \pm 0.02$
SO	99.299870	$N_J = 2_3 - 1_2$	$0.108 \pm 0.006$	$-46.71 \pm 0.16$	$6.3 \pm 0.4$	$0.751 \pm 0.019$
HC <sub>3</sub> N	100.076392	$J = 11 - 10$				< 0.07
C <sup>18</sup> O	109.782173	$J = 1 - 0$	$0.102 \pm 0.008$	$-46.86 \pm 0.19$	$5.1 \pm 0.4$	$0.58 \pm 0.02$
<sup>13</sup> CO	110.201354	$J = 1 - 0$	$1.25 \pm 0.02$	$-46.93 \pm 0.05$	$5.70 \pm 0.13$	$7.74 \pm 0.02$

NOTE—The errors are  $1\sigma$ . The upper limits are  $3\sigma$ . The calibration error ( $\sim 20\%$ ) is not included. A peak temperature ( $T_{\text{MB}}$  Peak), a peak velocity ( $v_{\text{LSR}}$ ), and a line width ( $\Delta v$ ) are obtained by gaussian fit to the spectrum averaged over the whole observed area (shown in Figure 5). Integrated intensities ( $\int T_{\text{MB}} dv$ ) are calculated in the velocity range from  $-57$  to  $-37$  km s<sup>-1</sup> except for HCN. For HCN, the velocity range is from  $-67$  to  $-27$  km s<sup>-1</sup> to cover all the hyperfine components.

### 3.2. Distribution of key molecular species

In order to characterize the chemical composition averaged over the 9.0 pc × 9.0 pc area, it is necessary to investigate which molecular emission comes from which part of the molecular cloud. We select the 11 strongest lines, CCH ( $N = 1 - 0$ ), HCN ( $J = 1 - 0$ ), HCO<sup>+</sup> ( $J = 1 - 0$ ), HNC ( $J = 1 - 0$ ), C<sup>34</sup>S ( $J = 2 - 1$ ), CH<sub>3</sub>OH ( $J_K = 2_K - 1_K$ ), CS ( $J = 2 - 1$ ), SO ( $J_K = 3_2 - 2_1$ ), HC<sub>3</sub>N ( $J = 11 - 10$ ), C<sup>18</sup>O ( $J = 1 - 0$ ), and <sup>13</sup>CO ( $J = 1 - 0$ ), and prepare their integrated intensity maps with the 30'' grid, as shown in Figure 6. This grid size

corresponds to the spatial scale of 0.28 pc at the distance of W3 (1.95 kpc). The velocity range of integration is from  $-57$  to  $-37$  km s<sup>-1</sup> except for HCN. For HCN, the velocity range is from  $-67$  to  $-27$  km s<sup>-1</sup> in order to cover all the hyperfine components. It should be noted that the velocity difference across the observed area is 4 km s<sup>-1</sup> at most, which is smaller than the range of integration mentioned above.

The distribution of <sup>13</sup>CO extends to the north-south direction, which is consistent with the <sup>13</sup>CO map previously reported by Sakai et al. (2006). The distribution of C<sup>18</sup>O is also consistent with the map by Sakai et al.

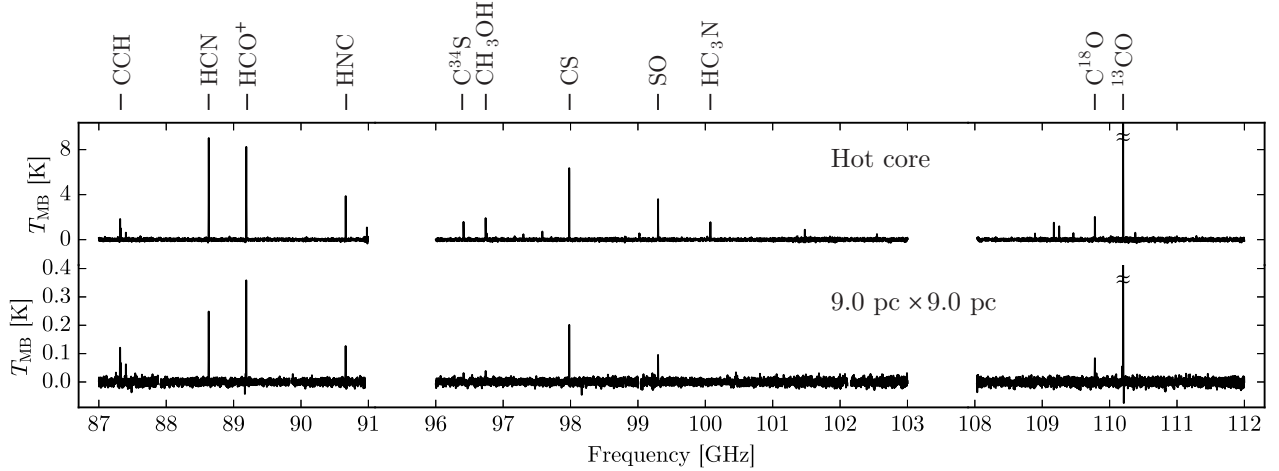


**Figure 3.** *Upper:* Spectrum of the W3(OH) hot core. *Lower:* The spectrum averaged over all the observed area (9.0 pc  $\times$  9.0 pc). The representative molecular lines are indicated on the top.

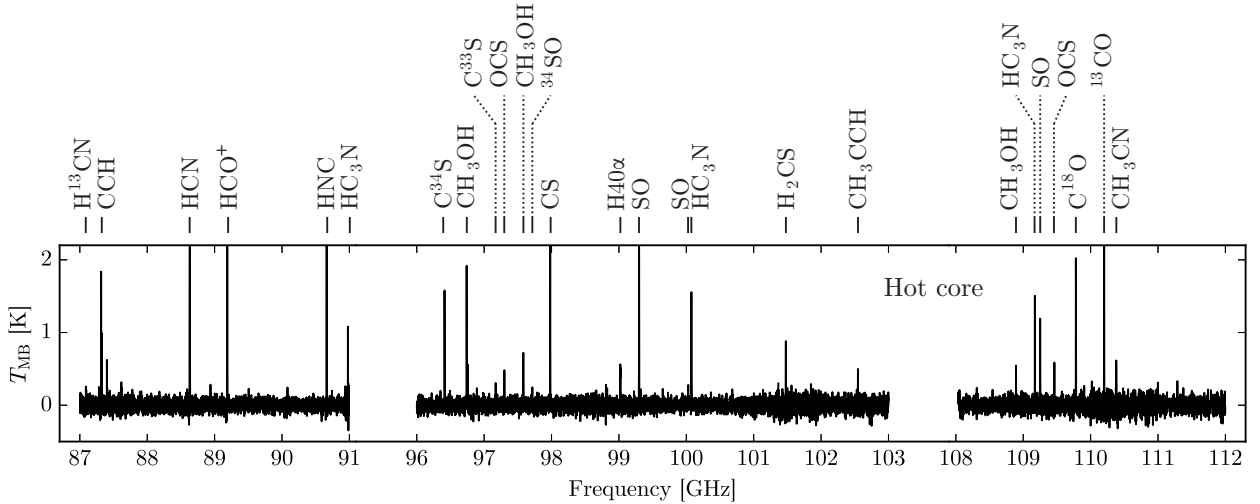


**Figure 4.** Zoomed spectrum of the W3(OH) hot core. The detected species are indicated on the top.

(2006), in spite of the rather poor signal-to-noise ratio of our  $C^{18}O$  data. All the distributions including these of  $^{13}CO$  and  $C^{18}O$  have a peak at the center position. However, the degree of concentration to the center differs from species to species. To evaluate the degree of concentration, we apply a two-dimensional Gaussian fit to integrated intensities. The parameters are summarized in Table 2. We can arbitrarily classify the distributions into the following three types; (i) species concentrated just around the center, such as  $CH_3OH$ ,  $SO$ , and  $HC_3N$ , (ii) species loosely concentrated around the center, such as  $HCN$ ,  $HCO^+$ ,  $HNC$ , and  $CS$ , and (iii) species extended widely, such as  $CCH$ ,  $C^{18}O$ , and  $^{13}CO$ .

Such a difference of the emitting region among molecular species is caused by excitation effects and chemical abundance variations. Although the critical density of

molecular line is an important factor to the difference, it cannot explain everything. Table 3 summarizes the critical density and the upper state energy of each spectral line. The  $HCN$  ( $J = 1 - 0$ ) line has the highest critical density among the lines listed in Table 3. However, it is not exactly true that the  $HCN$  line only reflects high density regions in the molecular-cloud-scale spectrum. In fact, the  $HCN$  emission is more extended than the emission of other molecular lines with lower critical densities. The  $HCN$  molecules can sub-thermally be excited even in a region below the critical density, and hence the  $HCN$  emission can come from such less dense regions in the observation beam to some extent, as far as  $HCN$  exists. This is indeed revealed for the Orion A molecular cloud by Kauffmann et al. (2017). Since the less dense part has a larger area of molecular clouds,

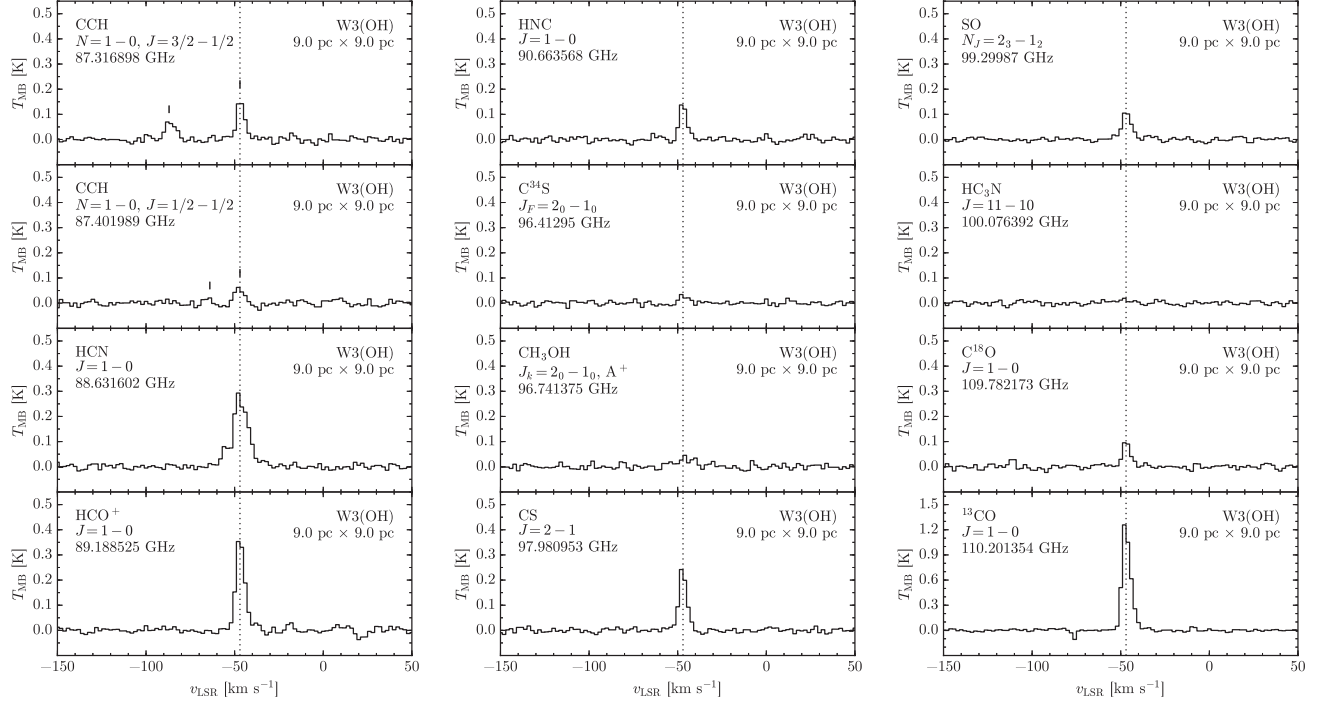


**Figure 5.** Spectral line profiles of individual molecular transitions in the spectrum averaged over the whole area ( $9.0 \text{ pc} \times 9.0 \text{ pc}$ ). The dashed lines indicate the velocity of  $-47 \text{ km s}^{-1}$ . Small vertical lines in the CCH panel represent the positions of the hyperfine components.

its contribution to the molecular-cloud-scale spectrum could overwhelm the contribution from the dense part. Needless to say, whether this situation happens also depends on the molecular abundance in each part. Thus, molecular-cloud-scale spectrum is also sensitive to chemical abundance variation, which is caused by various

factors such as the  $\text{H}_2$  density, the gas kinetic temperature, and the UV radiation field. This is the reason why we observationally study the molecular-cloud-scale spectrum by conducting mapping observations toward Galactic sources. We will discuss on this issue in Section 4.1.

**Table 2.** Spatial extent of key molecular species.

Molecule	Frequency (GHz)	Transition	Major axis (arcmin)	Minor axis (arcmin)	Position angle (deg)
CCH	87.316898	$N = 1 - 0, J = 5/2 - 3/2, F = 2 - 1$	4.2	2.0	30
$^{13}\text{CO}$	110.201354	$J = 1 - 0$	3.2	1.3	30
$\text{C}^{18}\text{O}$	109.782173	$J = 1 - 0$	2.8	1.1	30
$\text{HCO}^+$	89.188525	$J = 1 - 0$	2.2	1.3	30
HCN	88.631602	$J = 1 - 0$	1.9	1.2	30
CS	97.980953	$J = 2 - 1$	1.5	1.0	30
HNC	90.663568	$J = 1 - 0$	1.4	0.9	30
SO	99.299870	$N_J = 2_3 - 1_2$	1.2	0.7	30
$\text{C}^{34}\text{S}$	96.412950	$J_F = 2_0 - 1_0$	1.0	0.7	78
$\text{CH}_3\text{OH}$	96.741375	$J_K = 2_0 - 1_0, A^+$	1.0	0.6	33
$\text{HC}_3\text{N}$	100.076392	$J = 11 - 10$	0.7	0.4	55

NOTE—The FWHM values of major axis and minor axis are derived by the two-dimensional Gaussian fit. The position angle is measured from north through east.

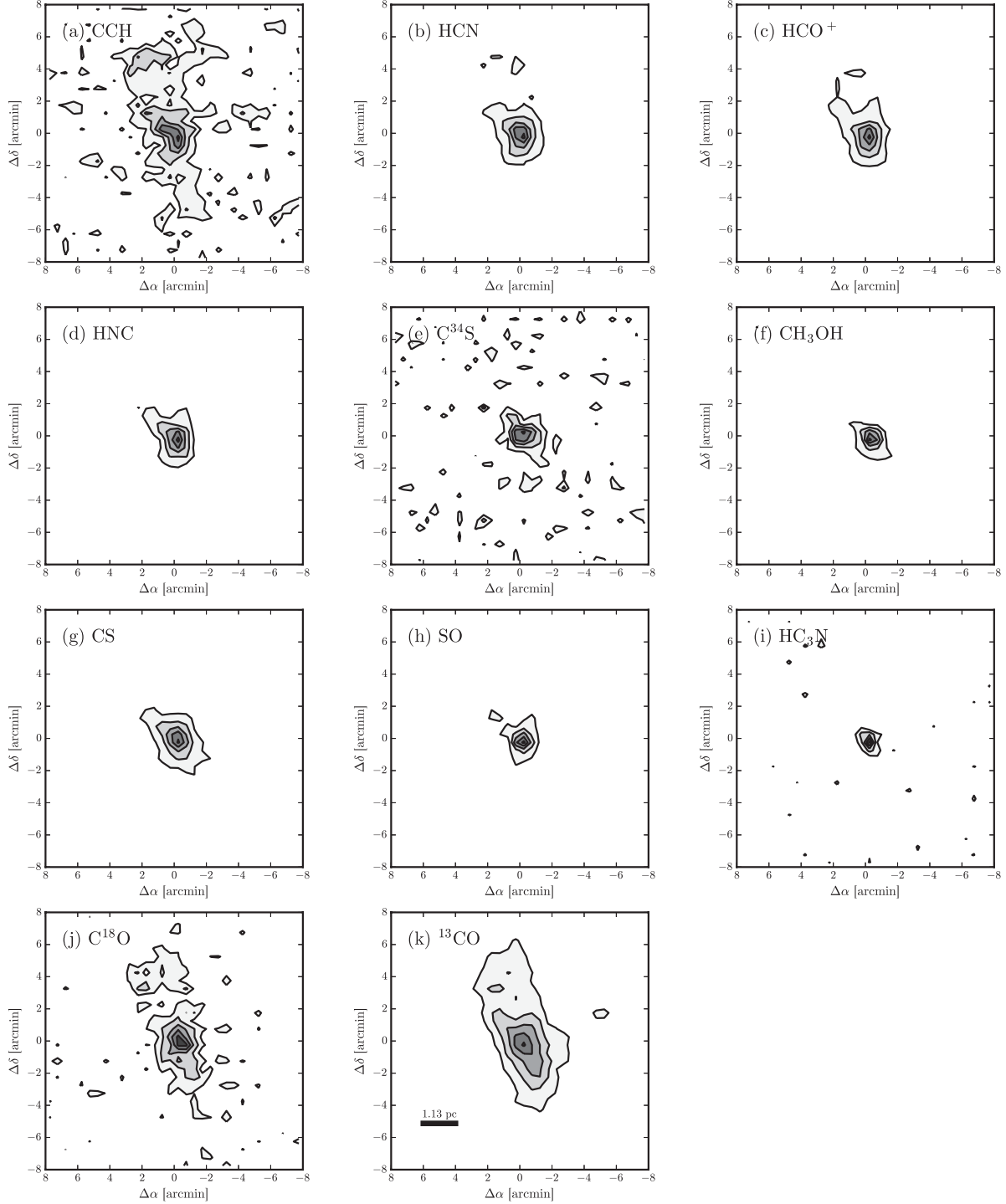


**Figure 6.** Integrated intensity maps of the bright emission lines. The coordinates ( $\Delta\alpha$ ,  $\Delta\delta$ ) are the offsets from W3(OH) ( $\alpha_{J2000.0} = 2^{\text{h}}27^{\text{m}}4.0^{\text{s}}$ ,  $\delta_{J2000.0} = 61^{\circ}52'24.0''$ ). The images are convolved to the  $30''$  resolution. The velocity range of integration is from  $-57$  to  $-37$   $\text{km s}^{-1}$  except for HCN. For HCN, the velocity interval is from  $-67$  to  $-27$   $\text{km s}^{-1}$  to cover all the hyperfine components. The contour levels are (20%, 40%, 60%, 80%, 100%) of (a)  $10$   $\text{K km s}^{-1}$ , (b)  $70$   $\text{K km s}^{-1}$ , (c)  $50$   $\text{K km s}^{-1}$ , (d)  $25$   $\text{K km s}^{-1}$ , (e)  $6$   $\text{K km s}^{-1}$ , (f)  $18$   $\text{K km s}^{-1}$ , (g)  $38$   $\text{K km s}^{-1}$ , (h)  $25$   $\text{K km s}^{-1}$ , (i)  $10$   $\text{K km s}^{-1}$ , (j)  $10$   $\text{K km s}^{-1}$ , and (k)  $90$   $\text{K km s}^{-1}$ .

**Table 3.** The critical density and upper state energy of each spectral line.

Molecule	Frequency (GHz)	Transition	$E_u$ (K)	$n_{crit}$ at 10 K ( $\text{cm}^{-3}$ )	$n_{crit}$ at 100 K ( $\text{cm}^{-3}$ )
CCH	87.316898	$N = 1 - 0, J = 5/2 - 3/2, F = 2 - 1$	4.2	$1.21 \times 10^5$	$1.94 \times 10^5$
HCN	88.631602	$J = 1 - 0$	4.3	$1.01 \times 10^6$	$2.66 \times 10^6$
HCO <sup>+</sup>	89.188525	$J = 1 - 0$	4.3	$1.64 \times 10^5$	$2.36 \times 10^5$
HNC	90.663568	$J = 1 - 0$	4.4	$2.77 \times 10^5$	$4.12 \times 10^5$
CH <sub>3</sub> OH	96.741375	$J_K = 2_0 - 1_0, A^+$	7.0	$3.10 \times 10^4$	$3.83 \times 10^4$
CS	97.980953	$J = 2 - 1$	7.1	$3.32 \times 10^5$	$3.84 \times 10^5$
SO	99.299870	$N_J = 2_3 - 1_2$	9.2	...	$2.95 \times 10^5$
HC <sub>3</sub> N	100.076392	$J = 11 - 10$	28.8	$8.83 \times 10^5$	...
H <sub>2</sub> CS	101.477810	$J_{K_p, K_o} = 3_{1,3} - 2_{1,2}$	22.9	$1.59 \times 10^5$	$1.77 \times 10^5$
OCS	109.463063	$J = 9 - 8$	26.3	$5.43 \times 10^4$	$4.56 \times 10^4$
C <sup>18</sup> O	109.782173	$J = 1 - 0$	5.3	$1.90 \times 10^3$	$1.80 \times 10^3$
<sup>13</sup> CO	110.201354	$J = 1 - 0$	5.3	$1.91 \times 10^3$	$1.80 \times 10^3$
CH <sub>3</sub> CN	110.383505	$J_K = 6_0 - 5_0$	18.5	...	$5.50 \times 10^5$

NOTE—The critical density  $n_{crit}$  is derived by  $A_{ij}/C_{ij}$ , where  $A_{ij}$  is the Einstein A-coefficient and  $C_{ij}$  is the collisional rate coefficient. These are adopted from the LAMDA database (van der Tak et al. 2007) and the original papers: CCH: Spielfiedel et al. (2012); HCN and HNC: Dumouchel et al. (2010); HCO<sup>+</sup>: Flower (1999); CH<sub>3</sub>OH: Rabli & Flower (2010); CS and SO: Lique et al. (2006); HC<sub>3</sub>N and OCS: Green & Chapman (1978); H<sub>2</sub>CS: Wiesenfeld & Faure (2013); C<sup>18</sup>O and <sup>13</sup>CO: Yang et al. (2010); CH<sub>3</sub>CN: Green (1986). For C<sup>34</sup>S, the collisional rates are not available in the LAMDA.

## 4. DISCUSSION

### 4.1. Correlation between the integrated intensities of molecules and <sup>13</sup>CO

As mentioned in Section 3.2, the distribution is different among the observed molecular species. In order to characterize the difference, we investigate correlations between the integrated intensities of <sup>13</sup>CO and those of various molecules. Here, we employ <sup>13</sup>CO as a reference molecule, because the <sup>13</sup>CO integrated intensity would roughly represent the line-of-sight column density of H<sub>2</sub>. Figure 7 shows the correlation diagrams. Each data point represents the integrated intensity averaged over a  $30'' \times 30''$  ( $0.28 \text{ pc} \times 0.28 \text{ pc}$ ) area. Consequently, the number of the data for the whole mapped area ( $16' \times 16'$ ) is 1024 in total. Note that the typical error of the integrated intensity at each data point is  $2 \text{ K km s}^{-1}$  ( $3\sigma$ ).

Roughly speaking, all diagrams show positive correlation. However, the dependence on the <sup>13</sup>CO integrated intensity is different from molecule to molecule, as expected from the variation of the molecular distributions. As shown in Figures 7e and 7h, the integrated intensities of CH<sub>3</sub>OH and HC<sub>3</sub>N seem to have an appearance threshold at the <sup>13</sup>CO integrated intensity of about  $40 \text{ K km s}^{-1}$  and  $60 \text{ K km s}^{-1}$ , respectively. The integrated intensities of C<sup>34</sup>S and SO gradually increase with the increasing <sup>13</sup>CO integrated intensity at  $I(^{13}\text{CO}) < 60 \text{ K km s}^{-1}$ , but the slope becomes steeper at a higher

<sup>13</sup>CO intensity (Figures 7d and 7g). These behaviors are consistent with the fact that the above four molecular species, CH<sub>3</sub>OH, HC<sub>3</sub>N, C<sup>34</sup>S, and SO, are mainly concentrated around the W3(OH) hot core (Figure 6).

The integrated intensities of HCN, HCO<sup>+</sup>, HNC, and CS start to rise with that of <sup>13</sup>CO more steeply than those of C<sup>34</sup>S and SO for  $I(^{13}\text{CO})$  less than  $40 \text{ K km s}^{-1}$  (Figures 7b, 7j, 7c, and 7f). However, their dependence on the <sup>13</sup>CO integrated intensity is not linear, but seems to have a knee point at the <sup>13</sup>CO integrated intensity of about  $40 - 60 \text{ K km s}^{-1}$ , above which the dependence becomes steeper. Similarity of these four species in their dependences on the <sup>13</sup>CO integrated intensity indicates their similar spatial distribution, as shown in Figure 6.

While the integrated intensities of most molecular species show non-linear dependences on the <sup>13</sup>CO integrated intensity, the integrated intensities of C<sup>18</sup>O and CCH increase almost linearly as the increasing <sup>13</sup>CO integrated intensity (Figures 7i and 7a). The linear correlation between C<sup>18</sup>O and <sup>13</sup>CO means that the <sup>13</sup>CO line is not optically very thick. In fact, the <sup>13</sup>CO/C<sup>18</sup>O ratio is approximately 10, which is consistent with the <sup>13</sup>C/<sup>18</sup>O ratio in the local interstellar medium ( $11 \pm 2$ ; Lucas & Liszt 1998). Hence, it is confirmed that the rapid increase of the integrated intensities of various molecules for the <sup>13</sup>CO integrated intensity higher than  $40 - 60 \text{ K km s}^{-1}$  does not mean the saturation of the <sup>13</sup>CO line. CCH also shows a linear correlation



with  $^{13}\text{CO}$ , although the signal-to-noise ratio is not very good. This result suggests that CCH is widely distributed over the molecular cloud as  $^{13}\text{CO}$ .

To quantitatively reveal the different behavior of the different species in Figure 7, we conduct a phenomenological fit to the correlation diagrams (Figure 8). Considering that most molecular species have a knee point around the  $^{13}\text{CO}$  integrated intensity of  $50 \text{ K km s}^{-1}$ , we employ two different linear functions for the ranges lower and higher than  $50 \text{ K km s}^{-1}$ . The slopes  $a_1$  and  $a_2$  shown in Figure 8 correspond to the fits for the lower and higher ranges, respectively. Hence, the  $a_2/a_1$  ratio roughly indicates how much the slope is increased from the lower range to the higher range: a larger  $a_2/a_1$  ratio means a larger change in the slope. While the  $a_2/a_1$  ratios of HCN,  $\text{HCO}^+$ , HNC, and CS are around 4, that of  $\text{CH}_3\text{OH}$ ,  $\text{HC}_3\text{N}$ ,  $\text{C}^{34}\text{S}$ , and SO are higher than 6. This result quantitatively shows a steeper increase of the intensities of  $\text{CH}_3\text{OH}$ ,  $\text{HC}_3\text{N}$ ,  $\text{C}^{34}\text{S}$ , and SO across the knee point. Note that this linear-function fitting is not based on any theoretical models, and the criteria of  $50 \text{ K km s}^{-1}$  is arbitrary.

For further investigations, similar correlation diagrams are prepared against the  $\text{HCO}^+$  integrated intensity instead of the  $^{13}\text{CO}$  integrated intensity (Figure 9). The integrated intensities of HCN, HNC, and CS are linearly correlated well, where the correlation coefficient is higher than 0.8 (Figures 9b, 9c, and 9f). This again verifies similar distributions of  $\text{HCO}^+$ , HCN, HNC, and CS. The integrated intensity of  $\text{CH}_3\text{OH}$ , SO, and  $\text{HC}_3\text{N}$  seem to have a knee point at the  $\text{HCO}^+$  integrated intensity of  $20 - 30 \text{ K km s}^{-1}$ , as seen as the appearance threshold in the correlation diagram with  $^{13}\text{CO}$  (Figures 9e, 9g, and 9h). A similar trend is marginally seen for  $\text{C}^{34}\text{S}$  (Figure 9d) in spite of the poor signal-to-noise ratio. On the other hand, the CCH and  $\text{C}^{18}\text{O}$  emissions are brightly observed even for the low  $\text{HCO}^+$  integrated intensity range (Figure 9a and 9i). The CCH and  $\text{C}^{18}\text{O}$  emission at the low  $\text{HCO}^+$  integrated intensity seem significant, because their noise levels are  $2 \text{ K km s}^{-1}$  ( $3\sigma$ ).

The emission from the extended gas with the low  $^{13}\text{CO}$  integrated intensity is generally faint, but the spatial area of such regions is much larger than that of dense cores. When the extended component is accumulated, it cannot be ignored in the averaged spectrum. In the following section, we examine the contributions of extended gas components and dense cores by classifying the observed area into 5 subregions according to the  $^{13}\text{CO}$  integrated intensity.

#### 4.2. 5 subregions and their characteristics

What does the spectrum averaged over the molecular cloud represent? To address this question, we classify the full mapped region into 5 subregions according to

the  $^{13}\text{CO}$  integrated intensity  $I(^{13}\text{CO})$ . A criteria for the classification is arbitrary, as summarized in Table 4. The classification point is set every  $20 \text{ K km s}^{-1}$ , considering the highest  $I(^{13}\text{CO})$  of  $93.5 \text{ K km s}^{-1}$ . The 5 subregions (A–E) are shown in Figure 10. The subregion A is just around the W3(OH) hot core, while subregions B, C, and D surround it, extending along north-south direction. The subregion E is the other remaining part.

Then, we prepare a spatially averaged spectrum of each subregion, as shown in Figure 11. The average integrated intensities in each subregion of key molecular species are summarized in Table 5. We see the spectral lines of CCH, HCN,  $\text{HCO}^+$ , HNC, CS, SO,  $\text{C}^{18}\text{O}$ , and  $^{13}\text{CO}$  in the spectra of all the subregions, but with different relative intensities. In the subregion E, HNC, SO, and  $\text{C}^{18}\text{O}$  are faint, and the spectrum is rather similar to the spectrum averaged over the whole area. On the other hand, molecular species seen in the “hot core” spectrum, such as  $\text{H}_2\text{CS}$ ,  $\text{CH}_3\text{CCH}$ , and OCS, are also detected in the spectrum of the subregion A. The lines of these species become fainter in the subregions B and C in this order, and are not detected in the subregion D.

We closely compare the relative intensities of the lines of the key molecular species: CCH, HCN,  $\text{HCO}^+$ , HNC,  $\text{C}^{34}\text{S}$ ,  $\text{CH}_3\text{OH}$ , CS, SO,  $\text{HC}_3\text{N}$ ,  $\text{C}^{18}\text{O}$ , and  $^{13}\text{CO}$ , and investigated their variation among 5 subregions. For this comparison, we use the  $\text{HCO}^+$  line, which is the second brightest after the  $^{13}\text{CO}$  line as a reference. It traces moderately denser area ( $n_{\text{H}_2} \gtrsim 10^4 \text{ cm}^{-3}$ ) than the  $^{13}\text{CO}$  line, where the lines of the above molecules can be excited sub-thermally. As seen in Figure 11, the intensity ratios of almost all the species relative to  $\text{HCO}^+$  become low from the subregion A to the subregion E in this order. The only exception is CCH. The CCH/ $\text{HCO}^+$  ratio becomes higher in the subregion E. Note that the CS/ $\text{HCO}^+$  and  $\text{C}^{18}\text{O}/\text{HCO}^+$  ratios are highest at the subregion B. This may be caused by the line opacity and/or the chemical effect such as photodissociation near the star-forming core.

The relatively high CCH/ $\text{HCO}^+$  ratio in the outer subregions is obviously related to the widespread distribution of CCH. CCH is considered to be abundant in a photon dominated region (PDR). Since  $\text{C}^+$  is rich in PDRs, CCH is efficiently produced from  $\text{C}^+$  in the gas phase (Fuente et al. 2008). PDRs are extended in cloud peripheries, and hence, CCH can be relatively abundant in the outer part of the cloud.

In Figure 11, we find some differences in the intensities of HCN,  $\text{HCO}^+$ , HNC, and CS, among the 5 subregions, although they look similar in Figures 6, 7, and 9. The intensity of these 4 species similarly behave in the subregions A–D. HCN, HNC, and CS lines become fainter relative to the  $\text{HCO}^+$  line from the subregion

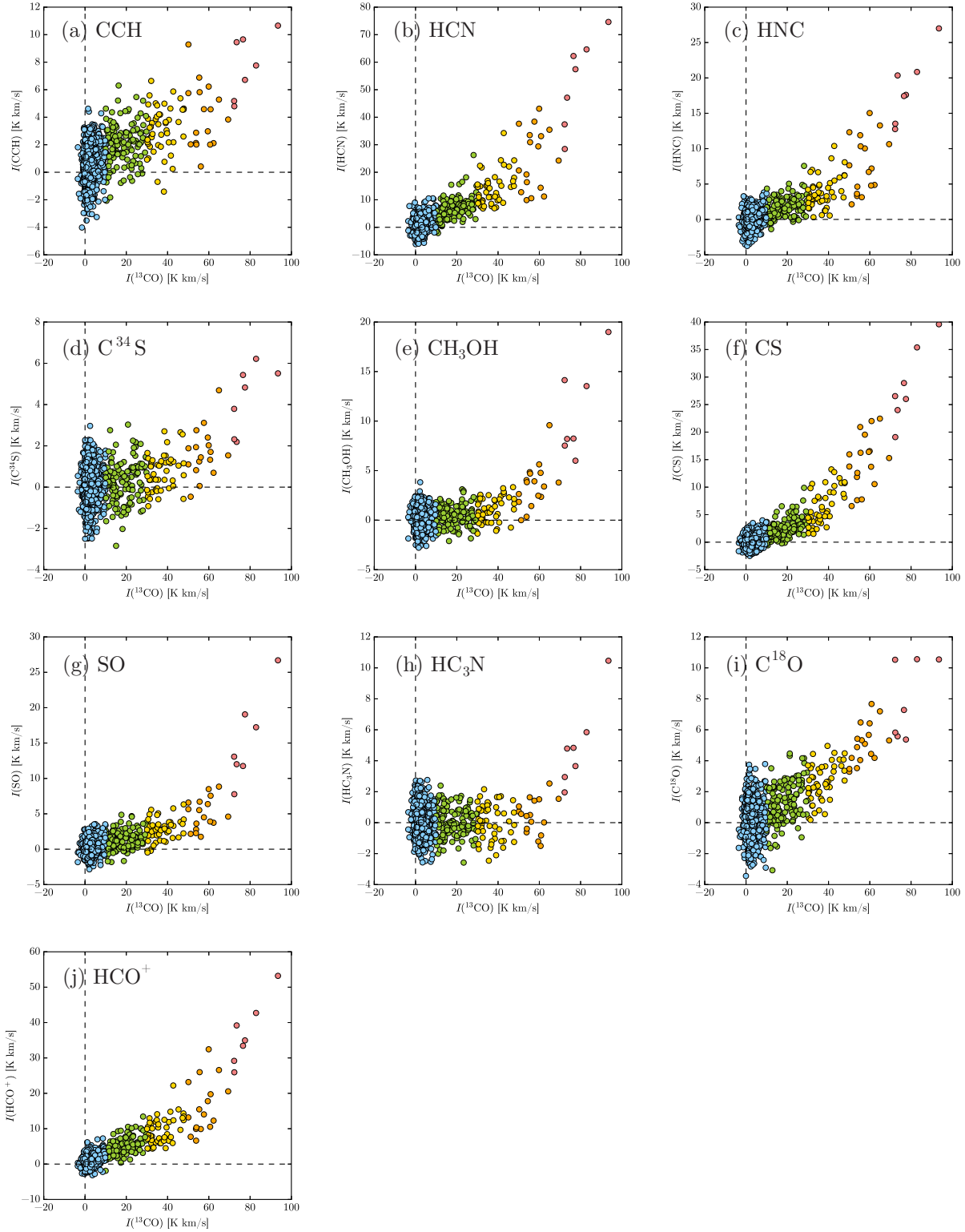


**Figure 7.** Correlation diagrams of integrated intensities of various molecules against that of  $^{13}\text{CO}$ . The velocity range of integration is from  $-57$  to  $-37$   $\text{km s}^{-1}$  except for HCN. For HCN, the velocity interval is from  $-67$  to  $-27$   $\text{km s}^{-1}$  to cover all the hyperfine components. The different colors indicate 5 subregions classified by the  $^{13}\text{CO}$  integrated intensity: *red*: subregion A ( $> 70$   $\text{K km s}^{-1}$ ), *orange*: subregion B ( $50 - 70$   $\text{K km s}^{-1}$ ), *yellow*: subregion C ( $30 - 50$   $\text{K km s}^{-1}$ ), *light green*: subregion D ( $10 - 30$   $\text{K km s}^{-1}$ ), and *light blue*: subregion E ( $< 10$   $\text{K km s}^{-1}$ ).

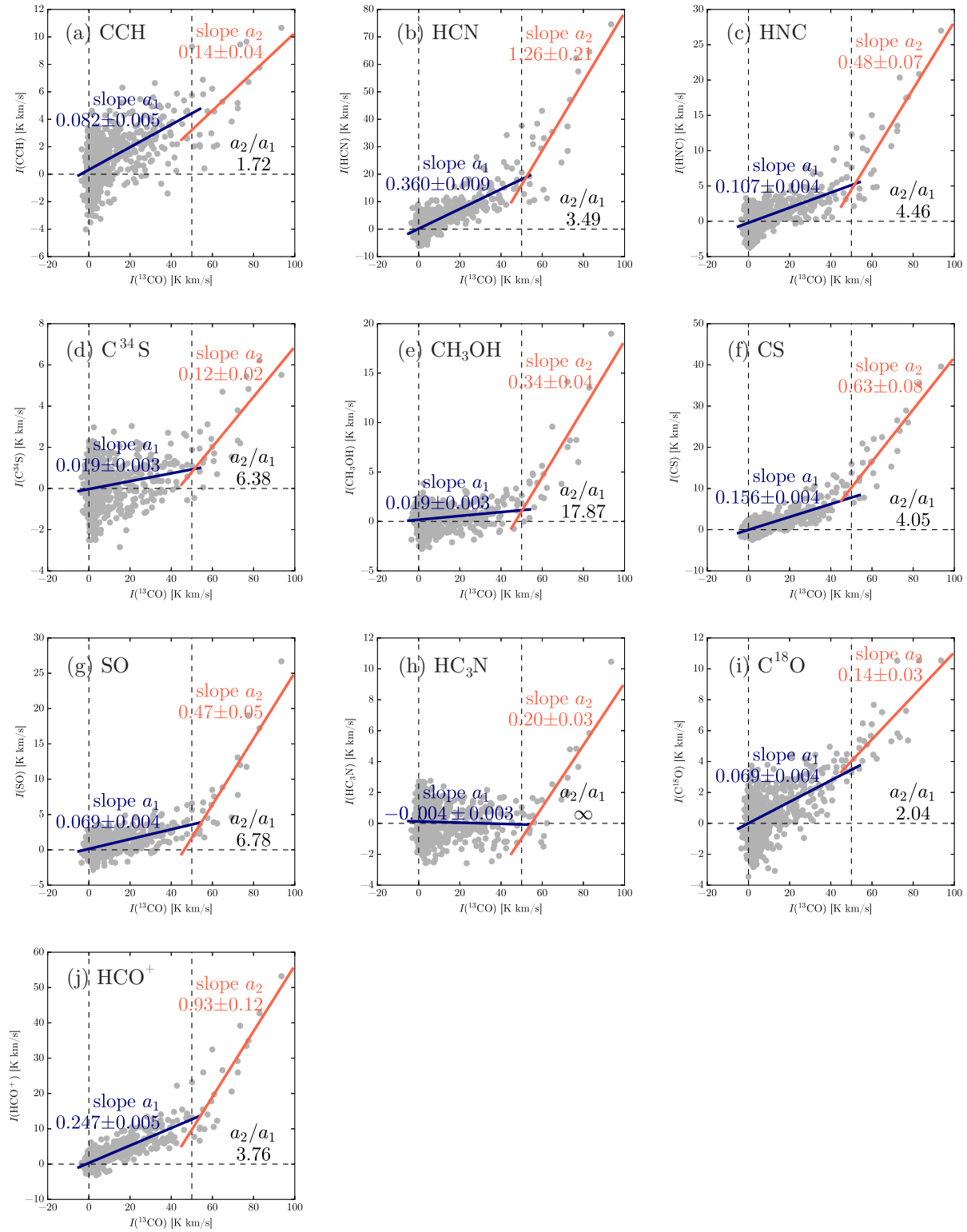


**Figure 8.** Same as the Figure 7, but with linear function fittings. Navy line is a linear function fitting for the data with the  $^{13}\text{CO}$  integrated intensities of  $< 50$  K km s $^{-1}$ , whereas orange-red line is that of  $> 50$  K km s $^{-1}$ . The slopes  $a_1$  and  $a_2$  correspond to the fits for  $< 50$  K km s $^{-1}$  and  $> 50$  K km s $^{-1}$ , respectively. The  $a_2/a_1$  ratio roughly indicates how much the slope is increased across the knee point ( $\sim 50$  K km s $^{-1}$ ): a larger  $a_2/a_1$  ratio means a larger change in the slope.

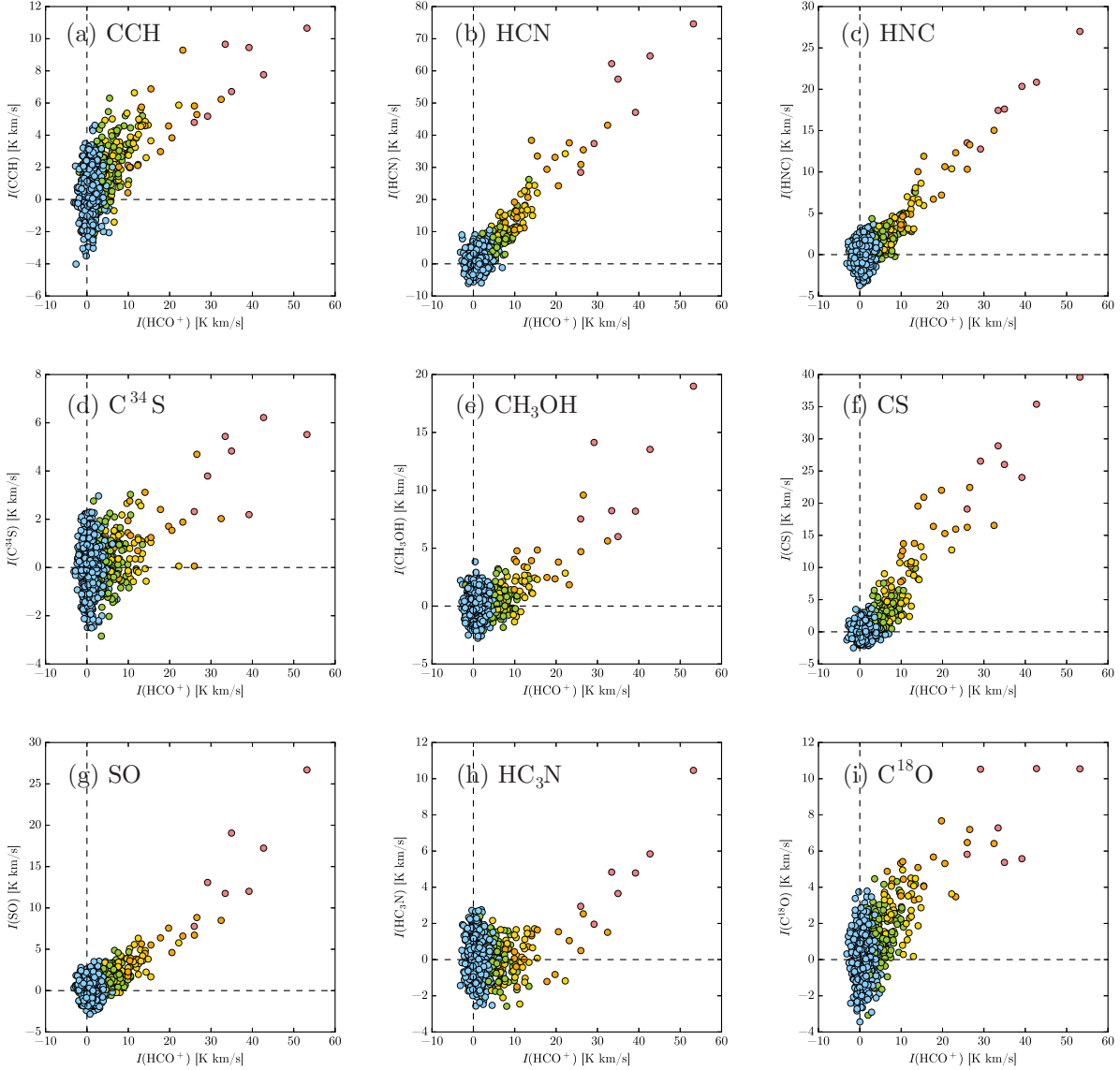


**Figure 9.** Correlation diagrams of integrated intensities of various molecules against that of  $\text{HCO}^+$ . The colors correspond to the subregions classified by the integrated intensity of  $^{13}\text{CO}$ . The velocity range of integration is from  $-57$  to  $-37$   $\text{km s}^{-1}$  except for HCN. For HCN, the velocity interval is from  $-67$  to  $-27$   $\text{km s}^{-1}$  to cover all the hyperfine components. The different colors indicate 5 subregions classified by the  $^{13}\text{CO}$  integrated intensity: *red*: subregion A ( $> 70$   $\text{K km s}^{-1}$ ); *orange*: subregion B ( $50 - 70$   $\text{K km s}^{-1}$ ); *yellow*: subregion C ( $30 - 50$   $\text{K km s}^{-1}$ ); *light green*: subregion D ( $10 - 30$   $\text{K km s}^{-1}$ ); and *light blue*: subregion E ( $< 10$   $\text{K km s}^{-1}$ ).

A to the subregion D. In the subregion E, the intensity of the HNC line is fainter by a factor of 10 than in the subregion D, while HCN,  $\text{HCO}^+$ , and CS lines are fainter by a factor of 5–7 than in the subregion D. The excitation effect does not seem responsible for the faintness of HNC in the subregion E. The critical density ( $n_{crit}$ ) of the HCN ( $J = 1 - 0$ ) line ( $1.0 \times 10^6$   $\text{cm}^{-3}$  at 10 K) is actually higher than that of the HNC ( $J = 1 - 0$ ) line ( $2.8 \times 10^5$   $\text{cm}^{-3}$  at 10 K), as shown in Table 3. Thus HNC is more deficient than HCN in the subregion E probably because of its formation and de-

struction processes. It is worth noting that HNC is less stable in energy than HCN by 0.64 eV (KIDA database; Wakelam et al. 2012), and hence, HNC is known to be isomerized to HCN under a high temperature condition ( $> 24$  K; Hirota et al. 1998). Since the subregion E is expected to have higher temperature due to penetration of the interstellar UV radiation, the isomerization would occur efficiently, resulting in deficiency of HNC there.

The detections of CCH, HCN,  $\text{HCO}^+$ , and CS in the subregion E indicate that the contribution of the extended gas may not be small for these molecular species

in the averaged spectrum. They are also observed in diffuse clouds in absorption against extragalactic continuum sources (Lucas & Liszt 1996, 2000; Liszt & Lucas 2001; Lucas & Liszt 2002). In the context of molecular-cloud-scale chemical compositions, Pety et al. (2017) reported that the diffuse and translucent gas contributes to the 45% or higher fluxes of CCH and  $\text{HCO}^+$  in their  $5.6 \text{ pc} \times 7.5 \text{ pc}$  observation toward Orion B giant molecular cloud, while it contributes the 30 – 40% fluxes of HCN and CS. Although a precise comparison is difficult, our result seems qualitatively consistent with theirs. This result suggests that the contribution of the translucent gas should be evaluated statistically in various environments in order to extract information about the dense gas from molecular-cloud-scale observations. Some works in this direction have recently been reported (e.g., Shimajiri et al. 2017; Kauffmann et al. 2017; Watanabe et al. 2017).

For a further analysis of the contribution of the extended gas, we prepare Figures 12 and 13, which reveals a fraction of the flux of each subregion relative to the total flux of the spectrum averaged over the whole area. In Figure 12, the fractional flux is defined as:

$$\text{Fractional Flux (\%)} = \frac{\sum_{i \in R} I_i(X)}{\sum_{i \in \text{All}} I_i(X)} \times 100\%,$$

where  $I_i(X)$  stands for the integrated intensity of a given molecule for the  $i$ -th  $30'' \times 30''$  area and R represents the subregions A, B, C, D, and E. “All” means the whole observed area. Likewise, the fractional area is defined as the number of the grids belonging to a given subregion divided by the total number of the grids. Figure 13 shows the spectral line profiles of individual molecular species, where the contribution from each subregion is indicated by colors. This figure is almost equivalent to Figure 12, but better represents the contribution of each subregion including the uncertainties due to the signal-to-noise ratio of the spectra.

In Figure 12, we confirm that the contribution of the subregion A to the whole-area spectrum is small for all the molecular species. In particular, the flux of CCH mostly comes from the outer subregions D and E. It is surprising that more than 1/3 of  $\text{CH}_3\text{OH}$  and SO flux come from the subregion E, although the emissions of these species look concentrated around the hot core, as seen in Figure 6. Note that the large flux of  $\text{HC}_3\text{N}$  coming from subregion E (Figure 12(i)) is likely affected by noise, as seen in Figure 13(i). The low-level emissions of  $\text{CH}_3\text{OH}$  and SO extended in cloud peripheries are notable, because these species are often thought as good tracers of shocks associated with star formation. However, these molecules are also known to reside in cold

dark clouds such as TMC-1 and L1544 (Takakuwa et al. 1998 and Bizzocchi et al. 2014, respectively), although their emissions are not as bright as those in star forming regions. Hence, accumulation of these weak emissions over a large area would make a significant contribution to the spectrum averaged over the whole area of W3(OH). This result gives an important implication for interpretation of the emissions of these molecules observed toward external galaxies in the 3 mm band.

**Table 4.** Classification of subregions.

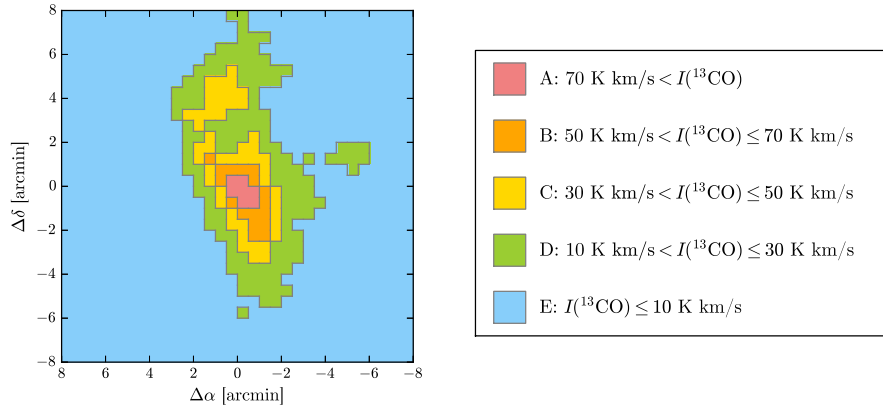
region	$I(^{13}\text{CO})$ (K km s $^{-1}$ )	number of data points	Area (arcmin $^2$ )
A	> 70	7	1.75
B	50 – 70	17	4.25
C	30 – 50	49	12.25
D	10 – 30	132	33.00
E	< 10	819	204.75

#### 4.3. Comparison with W51

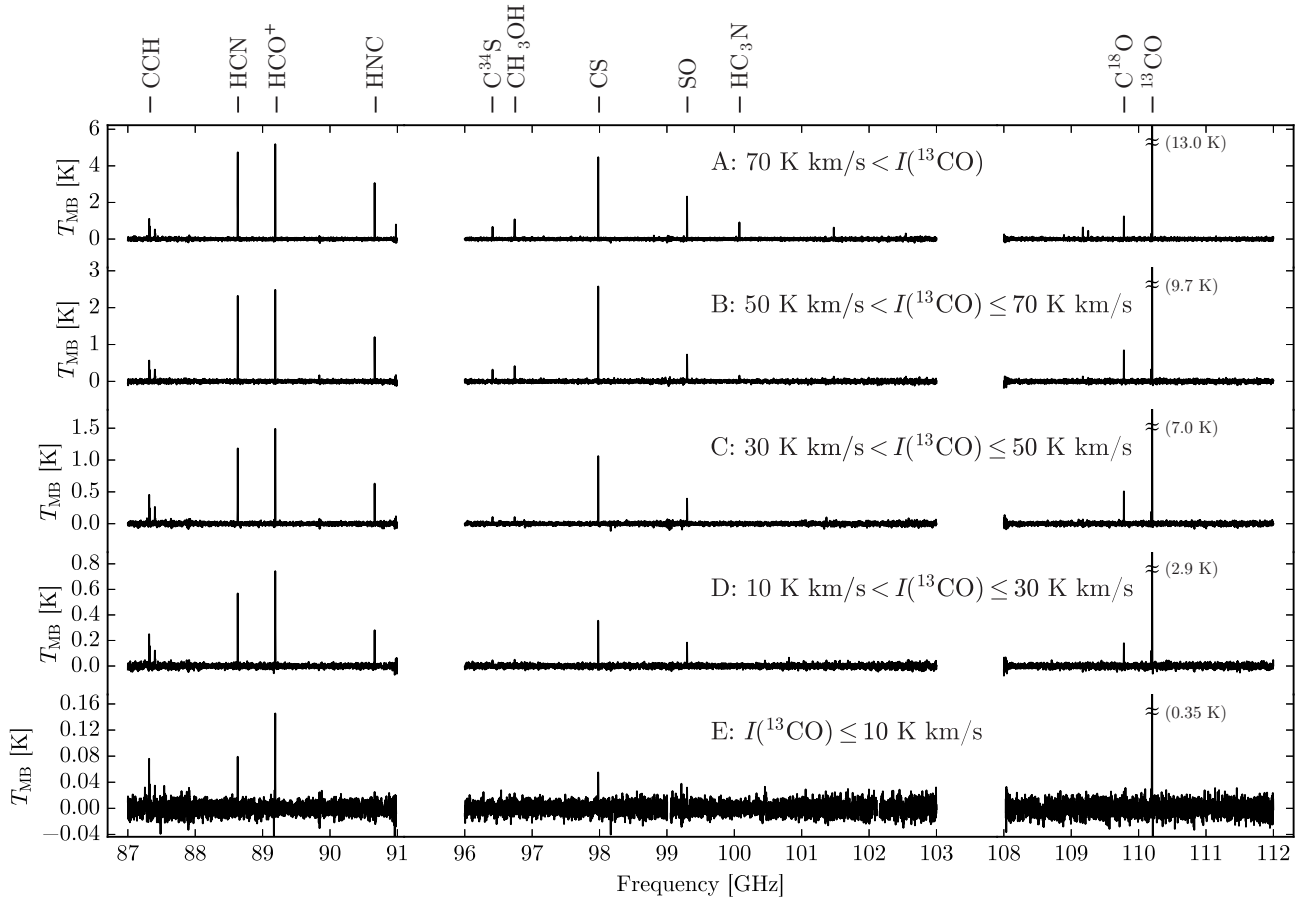
In the first paper of this series (Watanabe et al. 2017), we presented the mapping spectral line survey toward W51. W51 is a more active star-forming region than W3(OH). The cloud size of W51 is larger than that of W3(OH), and hence, the mapped area of W51,  $39 \text{ pc} \times 47 \text{ pc}$ , is larger than that for W3(OH) ( $9.0 \text{ pc} \times 9.0 \text{ pc}$ ). In spite of the large difference in the star-forming activity, the cloud size, and the location in the Milky Way, we find similarity of the spectra averaged over the observed area and the distributions of key molecular species between W3(OH) and W51.

Figure 14 shows the spectrum averaged over the whole area in W51. In the spatially averaged spectrum of W51, the lines of  $c\text{-C}_3\text{H}_2$ , CCH, HCN,  $\text{HCO}^+$ , HNC,  $\text{N}_2\text{H}^+$ ,  $\text{CH}_3\text{OH}$ , CS, SO,  $\text{C}^{18}\text{O}$ ,  $^{13}\text{CO}$ , and CN are detected. These molecular species are also identified in the spatially averaged spectrum of W3(OH) except for  $c\text{-C}_3\text{H}_2$ ,  $\text{N}_2\text{H}^+$  and CN, whose transitions are not covered in the present frequency settings. Furthermore, the spectral intensity pattern of W51 is similar to that of W3(OH) as a whole. Figure 15 shows a correlation diagram of integrated intensity ratios of CCH, HCN, HNC,  $\text{C}^{34}\text{S}$ ,  $\text{CH}_3\text{OH}$ , CS, SO,  $\text{C}^{18}\text{O}$ , and  $^{13}\text{CO}$  relative to  $\text{HCO}^+$  between W3(OH) and W51. Indeed, the correlation coefficient is 0.96 among 10 species: CCH, HCN,  $\text{HCO}^+$ , HNC,  $\text{C}^{34}\text{S}$ ,  $\text{CH}_3\text{OH}$ , CS, SO,  $\text{C}^{18}\text{O}$ , and  $^{13}\text{CO}$ . Even if  $^{13}\text{CO}$  is excluded, it is still as high as 0.85.

The similarity of the large-scale spectra of W51 and W3(OH) can further be confirmed, when we look at the



**Figure 10.** 5 subregions classified by the  $^{13}\text{CO}$  integrated intensity. The coordinates  $(\Delta\alpha, \Delta\delta)$  are the same as Figure 6.



**Figure 11.** Spectra of subregions A, B, C, D, and E. The apparent sizes of the  $\text{HCO}^+$  line intensity are presented to be identical among the panels. Note that the temperature scale of the spectrum is different from subregion to subregion.

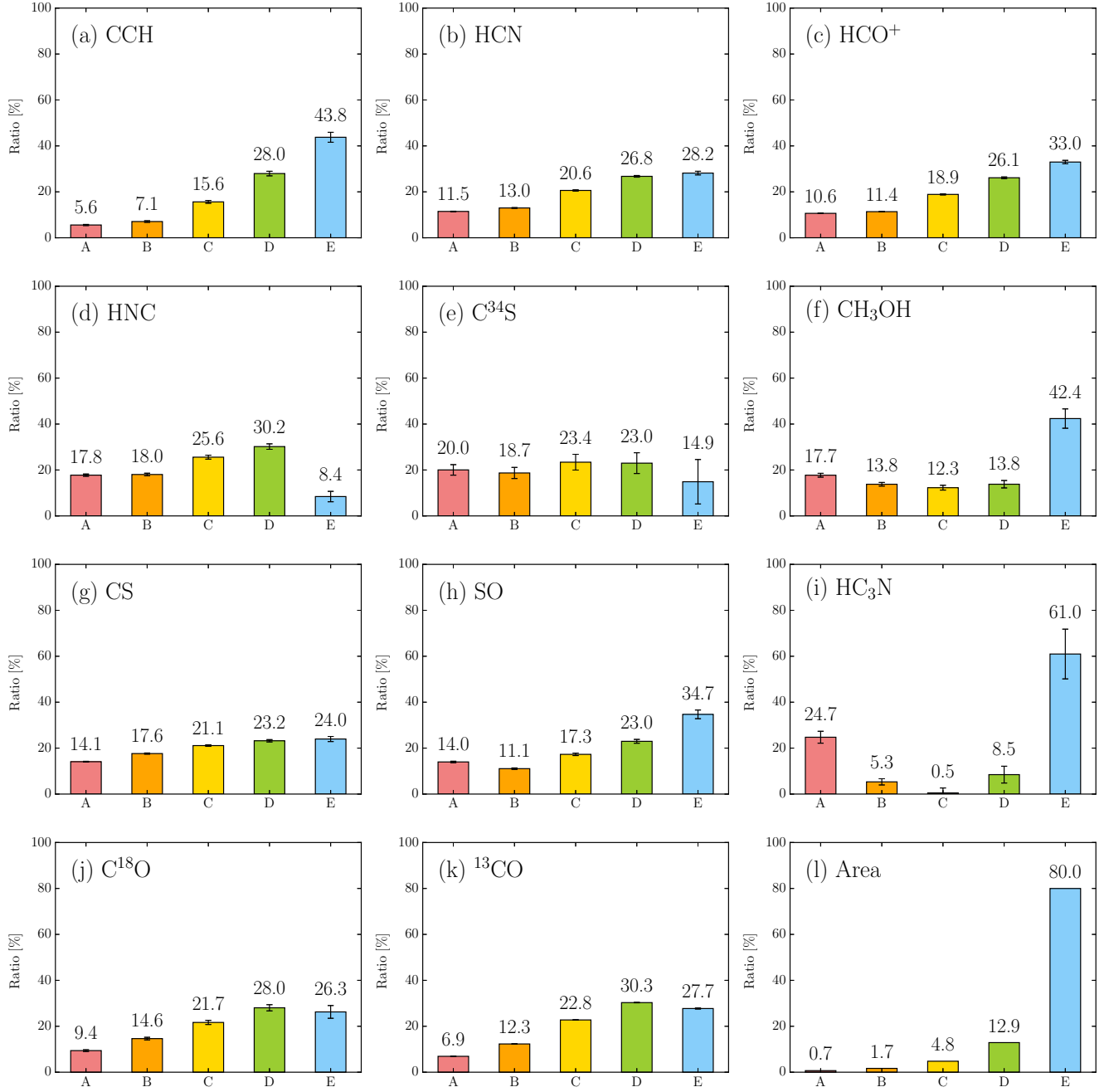


**Figure 12.** (a)-(k) Fractional fluxes of each species and (l) fractional area for 5 subregions. Black lines indicate errors ( $1\sigma$ ). A, B, C, D, and E are subregions classified by the <sup>13</sup>CO integrated intensity.

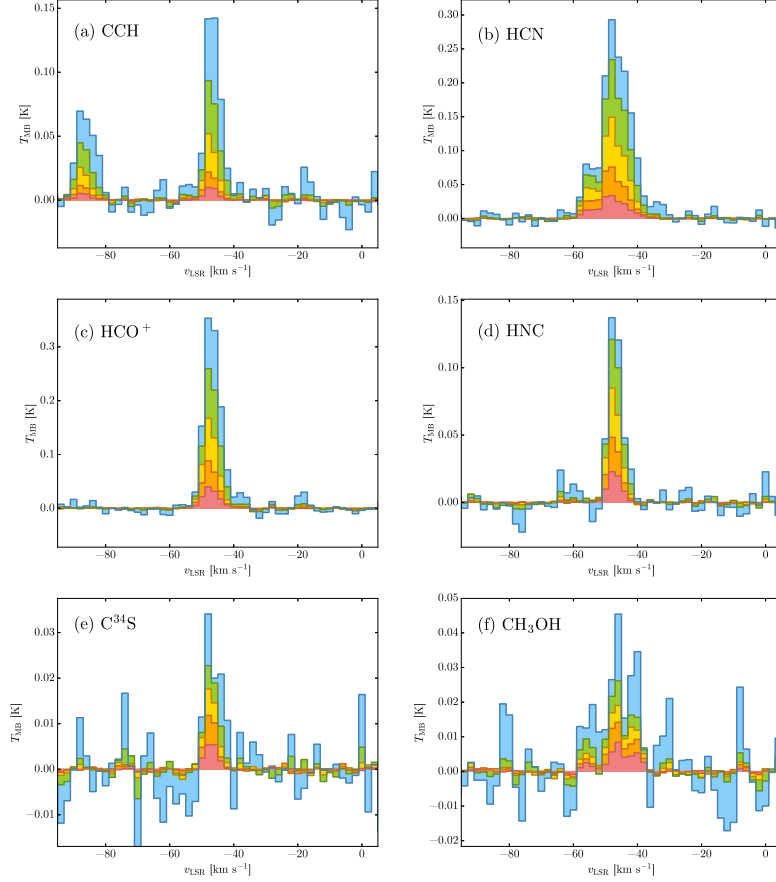


**Figure 13.** Spectral line profiles of individual molecular transitions in the spectrum averaged over the whole area ( $9.0 \text{ pc} \times 9.0 \text{ pc}$ ). Contributions from each subregion are calculated by multiplication of “flux from each subregion” by “fraction of the subregion in the whole area” and are indicated by color. Note that the spectra are summed up from the inner subregion (A) to the outer subregion (E), namely, red is of subregion A, orange is of subregion A+B, yellow is of subregion A+B+C, and so forth.

spectra of the subregions, fractional fluxes, and correlation plots of the integrated intensities of molecules against the  $^{13}\text{CO}$  integrated intensity. The characteristics discussed in Section 4.1 and 4.2 are also the case in W51; CCH is relatively bright in the outer subregion of the cloud, while the other molecular species become faint relative to  $\text{HCO}^+$  there.

The minor difference is seen in the subregion spectra of HCN and  $\text{C}^{18}\text{O}$ . In the case of W51, their intensity ratios relative to  $\text{HCO}^+$  are highest in the spectrum of the subregion C, while, in W3(OH), their intensity ra-

tios decrease toward the outer subregions. The possible reason is the effect of optical thickness, the arbitrariness of the dividing criteria and/or photodissociation nearby the star-forming core. In spite of these small differences, we stress that the chemical composition characteristic to the local star-forming cores is mostly smeared out in the molecular-cloud-scale chemical composition observed in the 3 mm band. Therefore, molecular-cloud-scale chemical compositions for the both sources are essentially similar to each other. Moreover, this result means that no apparent effect of the different galactocentric distances for these two sources can be seen.

**Table 5.** Average integrated intensities of each subregion.

Molecule	Frequency [GHz]	Transition	A (K km s <sup>-1</sup> )	B (K km s <sup>-1</sup> )	C (K km s <sup>-1</sup> )	D (K km s <sup>-1</sup> )	E (K km s <sup>-1</sup> )	9.0 pc × 9.0 pc averaged (K km s <sup>-1</sup> )
CCH	87.316898	$N = 1 - 0$ $J = 5/2 - 3/2$ $F = 2 - 1$	$7.7 \pm 0.4$	$4.0 \pm 0.2$	$3.11 \pm 0.12$	$2.06 \pm 0.07$	$0.52 \pm 0.03$	$0.95 \pm 0.03$

*Table 5 continued*



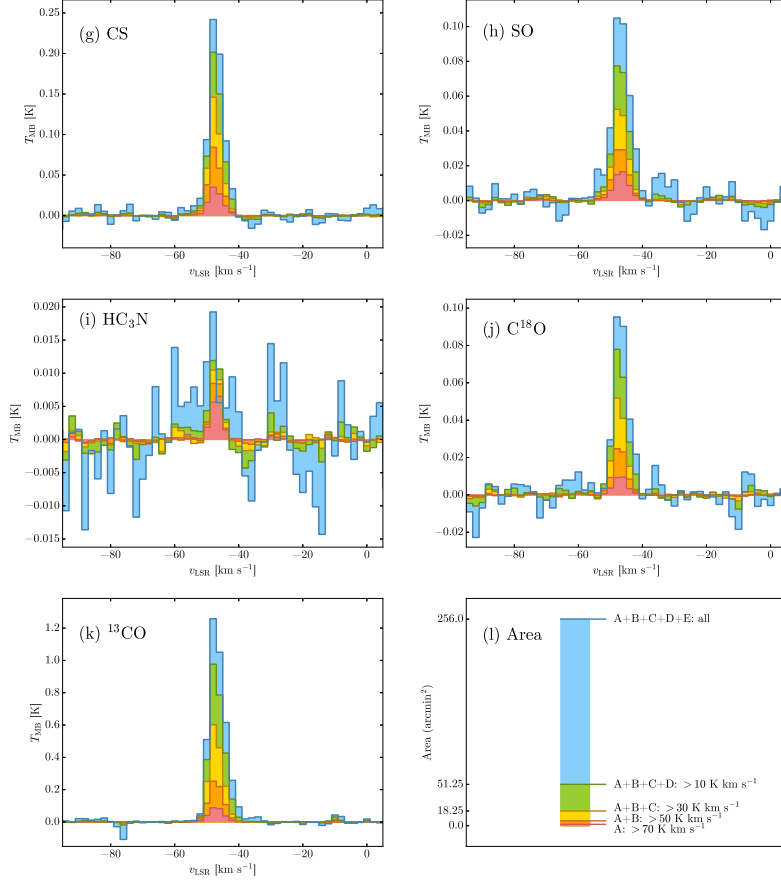


Figure 13. (continued)

Table 5 (continued)

Molecule	Frequency [GHz]	Transition	A (K km s <sup>-1</sup> )	B (K km s <sup>-1</sup> )	C (K km s <sup>-1</sup> )	D (K km s <sup>-1</sup> )	E (K km s <sup>-1</sup> )	9.0 pc × 9.0 pc averaged (K km s <sup>-1</sup> )
HCN	88.631602	1 – 0	53.1 ± 0.4	24.7 ± 0.3	13.63 ± 0.15	6.57 ± 0.09	1.11 ± 0.04	3.16 ± 0.03
HCO <sup>+</sup>	89.188525	1 – 0	36.9 ± 0.3	16.25 ± 0.19	9.37 ± 0.11	4.81 ± 0.07	0.98 ± 0.03	2.37 ± 0.02
HNC	90.663568	1 – 0	18.5 ± 0.3	7.74 ± 0.17	3.81 ± 0.10	1.67 ± 0.06	0.08 ± 0.02	0.71 ± 0.02
C <sup>34</sup> S	96.412950	2 <sub>0</sub> – 1 <sub>0</sub>	4.3 ± 0.2	1.66 ± 0.15	0.72 ± 0.09	0.26 ± 0.05	0.03 ± 0.02	0.148 ± 0.019
CH <sub>3</sub> OH	96.741375	2 <sub>0</sub> – 1 <sub>0</sub> , A <sup>+</sup>	10.9 ± 0.3	3.51 ± 0.16	1.08 ± 0.10	0.45 ± 0.06	0.22 ± 0.02	0.42 ± 0.02
CS	97.980953	2 – 1	28.5 ± 0.2	14.69 ± 0.15	6.10 ± 0.09	2.49 ± 0.06	0.41 ± 0.02	1.38 ± 0.02
SO	99.299870	N <sub>J</sub> = 2 <sub>3</sub> – 1 <sub>2</sub>	15.4 ± 0.2	5.01 ± 0.14	2.71 ± 0.09	1.34 ± 0.05	0.33 ± 0.02	0.751 ± 0.019
HC <sub>3</sub> N	100.076392	11 – 10	4.9 ± 0.2	0.44 ± 0.13	0.01 ± 0.08	0.09 ± 0.05	0.104 ± 0.019	0.136 ± 0.017
C <sup>18</sup> O	109.782173	1 – 0	8.0 ± 0.3	5.09 ± 0.16	2.62 ± 0.10	1.26 ± 0.06	0.19 ± 0.02	0.58 ± 0.02
<sup>13</sup> CO	110.201354	1 – 0	78.4 ± 0.3	57.36 ± 0.18	36.80 ± 0.10	18.19 ± 0.06	2.68 ± 0.03	7.74 ± 0.02

NOTE—The velocity intervals of integration are from  $-57$  to  $-37$  km s<sup>-1</sup> except for HCN. For HCN, the velocity range is from  $-67$  to  $-27$  km s<sup>-1</sup> to cover all the hyperfine components.

#### 4.4. Comparison with external galaxies

Spectral intensity patterns of external galaxies observed by single-dish telescopes are also ones averaged

over the molecular-cloud-scale. This is also true even for interferometer observations. The angular resolution readily achieved with the ALMA is about  $0.2''$ , which can be translated to the linear size of 10 pc for nearby

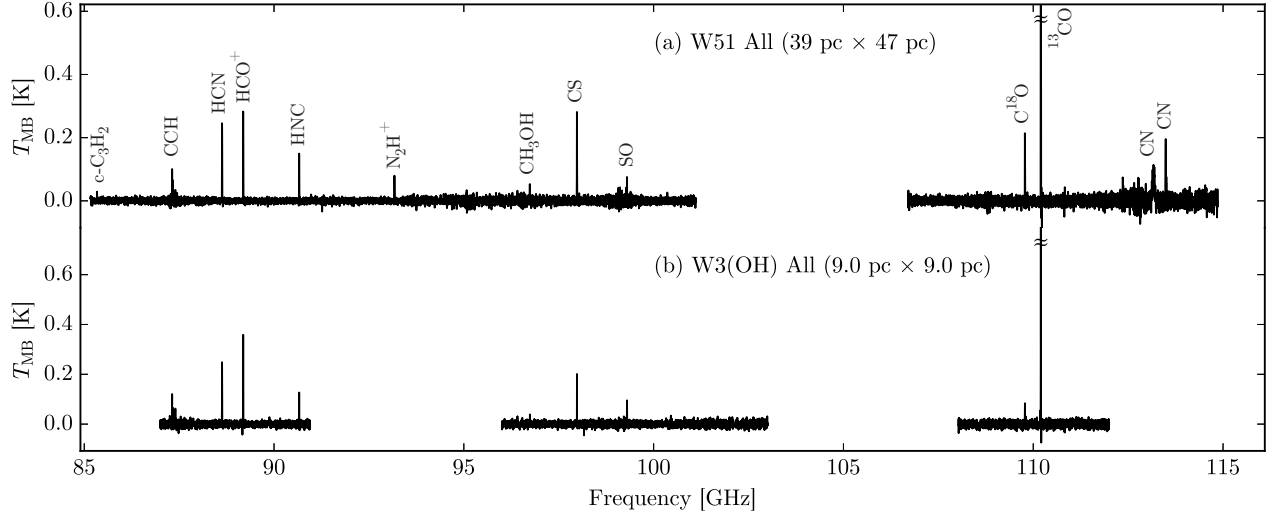


**Figure 14.** Spectra of (a) a averaged over the observed area in W51 presented by [Watanabe et al. \(2017\)](#) and (b) spectrum averaged over the observed area in W3(OH) for comparison.

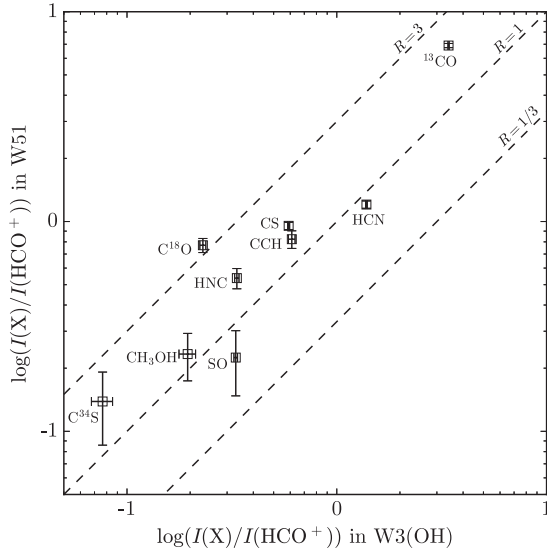


**Figure 15.** Correlation diagram of the integrated intensity ratios relative to that of  $\text{HCO}^+$  between W3(OH) (averaged over the  $9.0 \text{ pc} \times 9.0 \text{ pc}$  area) and W51 (averaged over the  $39 \text{ pc} \times 47 \text{ pc}$  area). The data for W51 is taken from [Watanabe et al. \(2017\)](#). Dashed lines indicate the ratios ( $R$ ) of 3, 1, and  $1/3$ .

galaxies at 10 Mpc. Hence, observed spectra toward external galaxies generally represent molecular-cloud-scale chemical composition.

We compare the integrated intensities of the bright molecular lines ( $\text{CCH}$  ( $N = 1 - 0$ ),  $\text{HCN}$  ( $J = 1 - 0$ ),  $\text{HCO}^+$  ( $J = 1 - 0$ ),  $\text{HNC}$  ( $J = 1 - 0$ ),  $\text{CH}_3\text{OH}$  ( $J_K = 2_K - 1_K$ ),  $\text{CS}$  ( $J = 2 - 1$ ),  $\text{SO}$  ( $J_K = 3_2 - 2_1$ ),  $\text{C}^{18}\text{O}$  ( $J = 1 - 0$ ), and  $^{13}\text{CO}$  ( $J = 1 - 0$ )) observed in W3(OH) with those observed in nearby galaxies. Fortunately, a fairly complete dataset of these molecular lines observed toward various kinds of galaxies in the 3 mm band is available in the literature. Figure 16 shows the integrated intensity ratios of molecules relative to  $\text{HCO}^+$  observed toward nearby galaxies. The values are normalized by that of the W3(OH) spectrum averaged over the  $9.0 \text{ pc} \times 9.0 \text{ pc}$  area. For this figure, we employ the data observed toward the spiral arm cloud (M51 P1), the central regions of the starburst galaxies (M83, NGC253, and M82), the active galactic nuclei (AGNs; M51 AGN, NGC1068, and NGC7469), the central regions of the ultra luminous infrared galaxies (ULIRGs; Arp220 and Mrk231) and the low-metallicity dwarf galaxies (the LMC N44C and IC10). The distances of these galaxies range from 50 kpc to 170 Mpc, and hence, the spatial resolutions range from 10 pc to

a few kpc. For the most species, the intensity ratios agree with that of W3(OH) within a factor of 3, as seen in Figure 16. This suggests that chemical compositions observed at a spatial resolution larger than 10 pc are generally similar, even if the spatial resolution is as large as a few kpc.

In spite of the general resemblance, some molecular species in a specific galaxy seem to be influenced by its environment, as summarized below:

- CCH: The CCH/HCO<sup>+</sup> ratio shows little variation among galaxies, and is close to the ratio for W3(OH). However, we note that the CCH/HCO<sup>+</sup> ratio seems to be enhanced in low-metallicity dwarf galaxies if the low elemental C/O ratio is considered (Nishimura et al. 2016a,b). As mentioned before, CCH is efficiently produced in PDRs. Hence, galaxies hosting larger PDRs could be advantageously rich in CCH. However, no apparent trend suggesting this picture is seen between starburst galaxies, which should be dominated by PDRs, and AGNs. One possibility is that the spectra of AGNs may also be contaminated by starburst regions owing to the coarse observation beam.
- HCN and HNC: The HCN/HCO<sup>+</sup> and HNC/HCO<sup>+</sup> ratios show relatively small variations from those for W3(OH) except for the low-metallicity galaxies, where both HCN and HNC tend to be less abundant due to the lower elemental N abundance (Nishimura et al. 2016a,b). In Arp220, HNC is by far abundant. This is already discussed by Aalto et al. (2007), who suggest the intensity enhancement of HNC caused by pumping of the rotational levels of HNC through the mid-infrared continuum and/or effects of X-ray Dominated Regions (XDRs).
- CH<sub>3</sub>OH: In the low-metallicity dwarf galaxies, CH<sub>3</sub>OH is not detected (upper limits are shown in Figure 16). The deficiency of CH<sub>3</sub>OH in the dwarf galaxies is explained by the lower abundance of dust grains and the intense UV radiation due to it (Nishimura et al. 2016a,b). In M82, CH<sub>3</sub>OH is still detectable, but the intensity is weak. This is consistent with the fact that M82 is heavily influenced by the intense UV radiation (Fuente et al. 2008).
- CS: The CS/HCO<sup>+</sup> ratio does not vary among galaxies, and is close to the ratio for W3(OH). Since the production and destruction processes of CS and HCO<sup>+</sup> are completely different, this trend may be fortuitous. However, this result might suggest the universal correlation between HCO<sup>+</sup> and

CS in molecular-cloud-scale chemical composition. Further statistical studies are awaited.

- SO: The SO/HCO<sup>+</sup> ratios are lower except for the low-metallicity dwarf galaxies than in W3(OH). The spatial resolutions are 10 pc and 80 pc for LMC N44C and IC10, respectively, while they are larger than several hundred pc for other galaxies. Hence, the SO/HCO<sup>+</sup> ratio may reflect the difference of a beam filling factor. It should be noted that SO is known to be enhanced by shocks due to outflows associated with protostars (e.g., Bachiller & Pérez Gutiérrez 1997). Such a contribution might affect molecular-cloud-scale spectra in the 3 mm band. Observations at a higher spatial resolution in the submillimeter-wave band will be useful to evaluate the contribution of such shocks.
- C<sup>18</sup>O and <sup>13</sup>CO: The ratio of C<sup>18</sup>O/HCO<sup>+</sup> and <sup>13</sup>CO/HCO<sup>+</sup> varies from galaxy to galaxy. In addition, no apparent correlation between C<sup>18</sup>O and <sup>13</sup>CO can be seen. The effects of elemental isotope abundances, optical depth, and isotope selective photodissociation can be responsible for this feature.

## 5. SUMMARY

We have conducted a mapping spectral line survey for the 9.0 pc × 9.0 pc area of the Galactic molecular cloud W3(OH) with the NRO 45 m telescope. The observed frequency ranges are 87 – 91, 96 – 103, and 108 – 112 GHz. The main results are summarized below.

(1) Eight molecular species, CCH, HCN, HCO<sup>+</sup>, HNC, CS, SO, C<sup>18</sup>O, and <sup>13</sup>CO, are identified in the spectrum averaged over all the observed area, while some molecular species such as OCS, H<sub>2</sub>CS, CH<sub>3</sub>CCH, and CH<sub>3</sub>CN detected in the hot core at a 0.17 pc resolution are missing in the averaged spectrum.

(2) In the spatially averaged spectrum, emission of the species concentrated just around the star-forming core, such as CH<sub>3</sub>OH is fainter than the hot core spectrum, whereas emission of the species widely extended over the cloud, such as CCH, is relatively stronger.

(3) We have classified the observed area into the 5 subregions according to the integrated intensity of <sup>13</sup>CO, and have evaluated the contribution of the molecular line flux of each subregion to the spectrum averaged over the whole observed area. It is suggested that the flux from the outer subregions (cloud peripheries) is not negligible even for the centrally concentrated species CH<sub>3</sub>OH.

(4) CCH, HCN, HCO<sup>+</sup>, and CS are still strongly detected in the spectrum of the region with the <sup>13</sup>CO integrated intensity lower than 10 K km s<sup>-1</sup>. Hence, the

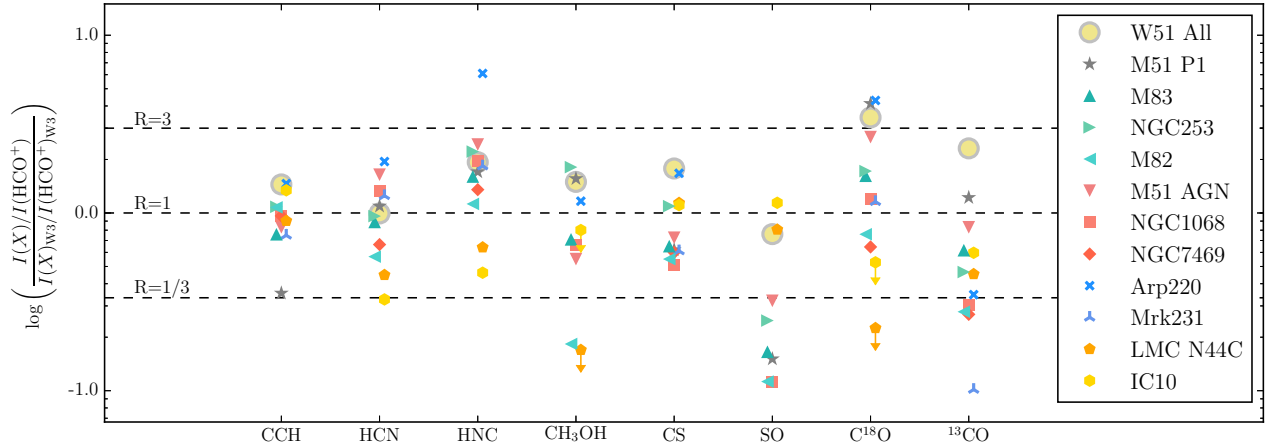


**Figure 16.** Integrated intensity ratios of molecules relative to  $\text{HCO}^+$  observed toward nearby galaxies. The values are normalized by that of  $\text{W3(OH)}$  (averaged over the  $9.0 \text{ pc} \times 9.0 \text{ pc}$  area). Dashed lines indicate the ratios ( $R$ ) of 3, 1, and  $1/3$  relative to  $\text{W3(OH)}$ . Integrated intensities are taken from the literature: W51 All (Galactic molecular cloud, averaged over the  $39 \text{ pc} \times 47 \text{ pc}$  area): [Watanabe et al. \(2017\)](#); M51 P1 (spiral arm): [Watanabe et al. \(2014\)](#); LMC N44C: [Nishimura et al. \(2016b\)](#); IC10: [Nishimura et al. \(2016a\)](#); and others: [Aladro et al. \(2015\)](#).

contribution of the extended gas is indeed significant. The spectrum averaged over the molecular-cloud scale in the 3 mm band seems to represent the gas extended around the star-forming core, rather than star-forming regions.

(5) The averaged spectrum is similar to the spectrum of the other Galactic molecular cloud W51 averaged over the  $39 \text{ pc} \times 47 \text{ pc}$  area, and also to the spectra observed in the external galaxies. The average spectrum can be regarded as the representative one, which is almost common in various molecular clouds.

(6) Molecular line intensity ratios are compared with those for the Galactic molecular cloud W51 and the 10 external galaxies. Most intensity ratios agree with that of  $\text{W3(OH)}$  within a factor of 3. Especially, the

$\text{CCH}/\text{HCO}^+$  and  $\text{CS}/\text{HCO}^+$  ratios show little variation among galaxies. On the other hand, the  $\text{CH}_3\text{OH}/\text{HCO}^+$  ratio tends to be low in dwarf galaxies and M82, probably due to the intense UV radiation. The  $\text{C}^{18}\text{O}/\text{HCO}^+$  and  $^{13}\text{CO}/\text{HCO}^+$  ratios seem to be affected by elemental isotope abundances, optical depth effects, and isotope selective photodissociation.

We are grateful to the anonymous reviewer for valuable comments and suggestions. We thank the staff of the NRO 45 m telescope for excellent support. This study is partly supported from Grants-in-Aid of Education, Sports, Science, and Technologies of Japan (21224002, 25400223, and 25108005). Y.N. is supported by Grant-in-Aid for JSPS Fellows (268280).

*Software:* NOSTAR, NEWSTAR

## REFERENCES

- Aalto, S., Spaans, M., Wiedner, M. C., & Hüttemeister, S. 2007, *A&A*, 464, 193
- Aladro, R., Viti, S., Bayet, E., et al. 2013, *A&A*, 549, A39
- Aladro, R., Martín, S., Riquelme, D., et al. 2015, *A&A*, 579, A101
- Bachiller, R., & Pérez Gutiérrez, M. 1997, *ApJL*, 487, L93
- Bizzocchi, L., Caselli, P., Spezzano, S., & Leonardo, E. 2014, *A&A*, 569, A27
- Dumouchel, F., Faure, A., & Lique, F. 2010, *MNRAS*, 406, 2488
- Flower, D. 1999, *MNRAS*, 305, 651
- Fuente, A., García-Burillo, S., Usero, A., et al. 2008, *A&A*, 492, 675
- Green, S. 1986, *ApJ*, 309, 331
- Green, S., & Chapman, S. 1978, *ApJS*, 37, 169
- Hirota, T., Yamamoto, S., Mikami, H., & Ohishi, M. 1998, *ApJ*, 503, 717
- Kauffmann, J., Goldsmith, P. F., Melnick, G., et al. 2017, *A&A*, in press, arXiv:1707.05352
- Kim, S.-J., Kim, H.-D., Lee, Y., et al. 2006, *ApJS*, 162, 161
- Lada, C. J., Elmegreen, B. G., Cong, H.-I., & Thaddeus, P. 1978, *ApJL*, 226, L39
- Lique, F., Spielfeldel, A., & Cernicharo, J. 2006, *A&A*, 451, 1125
- Liszt, H., & Lucas, R. 2001, *A&A*, 370, 576
- Lucas, R., & Liszt, H. 1996, *A&A*, 307, 237
- Lucas, R., & Liszt, H. 1998, *A&A*, 337, 246
- Lucas, R., & Liszt, H. S. 2000, *A&A*, 358, 1069
- . 2002, *A&A*, 384, 1054
- Martín, S., Mauersberger, R., Martín-Pintado, J., Henkel, C., & García-Burillo, S. 2006, *ApJS*, 164, 450

- Martín, S., Krips, M., Martín-Pintado, J., et al. 2011, *A&A*, 527, A36
- Müller, H. S., Schlöder, F., Stutzki, J., & Winnewisser, G. 2005, *Journal of Molecular Structure*, 742, 215
- Müller, H. S. P., Thorwirth, S., Roth, D. A., & Winnewisser, G. 2001, *A&A*, 370, L49
- Nagy, Z., van der Tak, F. F. S., Fuller, G. A., & Plume, R. 2015, *A&A*, 577, A127
- Nishimura, Y., Shimonishi, T., Watanabe, Y., et al. 2016a, *ApJ*, 829, 94
- . 2016b, *ApJ*, 818, 161
- Pety, J., Guzmán, V. V., Orkisz, J. H., et al. 2017, *A&A*, 599, A98
- Rabli, D., & Flower, D. 2010, *MNRAS*, 406, 95
- Rivera-Ingraham, A., Martin, P. G., Polychroni, D., et al. 2013, *ApJ*, 766, 85
- Sakai, T., Oka, T., & Yamamoto, S. 2006, *ApJ*, 649, 268
- Sato, M., Reid, M., Brunthaler, A., & Menten, K. 2010, *ApJ*, 720, 1055
- Shimajiri, Y., André, P., Braine, J., et al. 2017, *A&A*, 604, A74
- Spielfiedel, A., Feautrier, N., Najjar, F., et al. 2012, *MNRAS*, 421, 1891
- Takakuwa, S., Mikami, H., & Saito, M. 1998, *ApJ*, 501, 723
- van der Tak, F., Black, J. H., Schöier, F., Jansen, D., & van Dishoeck, E. F. 2007, *A&A*, 468, 627
- Wakelam, V., Herbst, E., Loison, J.-C., et al. 2012, *ApJS*, 199, 21
- Watanabe, Y., Nishimura, Y., Harada, N., et al. 2017, *ApJ*, 845, 116
- Watanabe, Y., Sakai, N., Sorai, K., & Yamamoto, S. 2014, *ApJ*, 788, 4
- Watanabe, Y., Sakai, N., López-Sepulcre, A., et al. 2015, *ApJ*, 809, 162
- Wiesenfeld, L., & Faure, A. 2013, *MNRAS*, 432, 2573
- Wynn-Williams, C. G., Becklin, E. E., & Neugebauer, G. 1972, *MNRAS*, 160, 1
- Wyrowski, F., Schilke, P., Walmsley, C. M., & Menten, K. M. 1999, *ApJL*, 514, L43
- Xu, Y., Reid, M., Zheng, X., & Menten, K. 2006, *Science*, 311, 54
- Yang, B., Stancil, P., Balakrishnan, N., & Forrey, R. 2010, *ApJ*, 718, 1062